Article

Estrogen enforces the integrity of blood vessels in the bone during pregnancy and menopause

Julia Rodrigues[1,2], Yi-Fang Wang[3], Amit Singh [4,5], Michelle Hendriks[1,2], Gopuraja Dharmalingam[3], Martine Cohen-Solal[6], Anjali P. Kusumbe[4] and Saravana K. Ramasamy [1,2]✉

The mammalian skeletal system shows sex differences in structure, functions, aging and disease incidences. The role of blood vessels in physiological, regenerative and pathological bone functions indicates the requisite to understanding their sex specificity. In this study, we found that estrogen regulates blood vessel physiology during pregnancy and menopause through estrogen receptor alpha (ERα) and G-protein-coupled estrogen receptor-1 (GPER1) but not ERβ-dependent signaling in mice. Estrogen regulates the lipid use of bone endothelial cells (BECs) and promotes lipolysis of adipocytes and fatty acid (FA) uptake from the microenvironment. Low estrogen conditions skew endothelial FA metabolism to accumulate lipid peroxides (LPOs), leading to vascular aging. High ferrous ion levels in female BECs intensify LPO accumulation and accelerate the aging process. Notably, inhibiting LPO generation using liproxstatin-1 in aged mice significantly improved bone heath. Thus, our findings demonstrate the effects of estrogen on BECs and suggest that LPO targeting could be an efficient strategy to manage blood and bone health in females.

Changes in the skeletal system during puberty, pregnancy and menopause are controlled by sex hormones that directly or indirectly regulate physiological and pathological bone remodeling[1,2]. The role of sex hormones on mesenchymal cells and hematopoietic cells has been well-recognized[3,4]. Despite playing a central role in skeletal physiology by regulating development, repair, aging and disease[5–7], the extent to which blood vessel functions differ between sexes remains poorly understood. In this study, we investigated blood vessel changes during pregnancy and menopause as well as the role of steroid hormones in mediating the growth and aging of BECs.

Vascular changes in bone during pregnancy and menopause

To understand cellular changes in the maternal bone microenvironment (BM) during pregnancy, we analyzed the tibia of pregnant mice on different days post-coitum (dpc) using improved imaging methods[8]. We used endomucin (Emcn) and CD31 to label blood vessels, osterix to mark early osteoblast lineage (OBL) cells and perilipin to identify adipocytes in the BM. CD31^{high}/Emcn^{high}-expressing type-H capillaries are angiogenic blood vessels that support osteogenesis in the bone[9,10]. We observed a notable increase in type-H vessels and

[1]Institute of Clinical Sciences, Imperial College London, London, UK. [2]MRC London Institute of Medical Sciences, Imperial College London, London, UK. [3]Bioinformatics and Computing Facility, MRC London Institute of Medical Sciences, Imperial College London, London, UK. [4]Tissue and Tumor Microenvironments Group, MRC Human Immunology Unit, MRC Weatherall Institute of Molecular Medicine, University of Oxford, Oxford, UK. [5]Heidelberg University Biochemistry Center, University of Heidelberg, Heidelberg, Germany. [6]Bioscar Inserm U1132 and Université de Paris, Hospital Lariboisiere, Paris, France. ✉e-mail: s.ramasamy@imperial.ac.uk
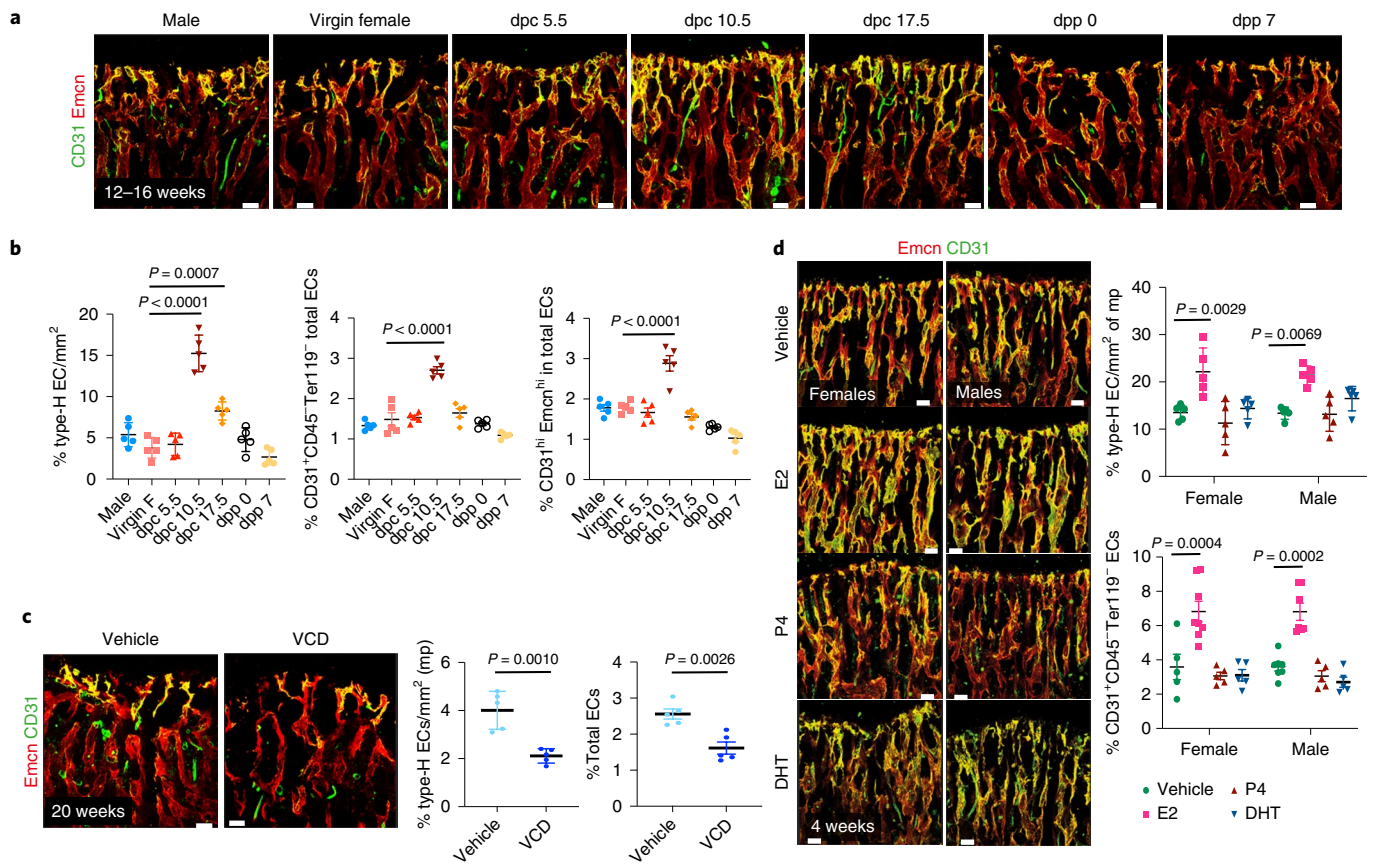
Fig. 1 | Estrogen regulates blood vessel growth in bones. a, Representative confocal images of type-H (Emcn^high/CD31^high) vessel changes in maternal bones at different timepoints of mouse pregnancy and post-delivery. Pregnancy timepoints are represented in days post-coitum (dpc) and post-delivery days as days post-partum (dpp). Scale bars, 40 μm. **b**, Quantification of type-H vessels described in **a**, as area of type-H ECs normalized to area of metaphysis (mp) (*n* = 5); total ECs (CD31⁺CD45⁻Ter119⁻) and type-H ECs (CD31^high/Emcn^high) are characterized by flow cytometry (*n* = 5). Data are mean ± s.d. for image quantification and mean ± s.e.m. for flow cytometry data; one-way ANOVA with Tukey's test. **c**, Representative confocal images of vehicle and VCD (*n* = 5) model mice (20 weeks old) depicting reduced type-H vessels in the VCD model. Scale bars, 40 μm. Graphs indicate the area of type-H ECs normalized to the area of mp and total ECs quantified by flow cytometry. Data are mean ± s.d. for image quantification and mean ± s.e.m. for flow cytometry data; unpaired two-tailed *t*-test. **d**, Representative confocal images showing changes in type-H vessels in male and female mice (P28) upon hormonal treatments with quantification for type-H ECs and area quantification (*n* = 5); flow cytometry (vehicle *n* = 5F, *n* = 7 M; E2 *n* = 8F, *n* = 7 M; P4 *n* = 5 F, *n* = 5 M; DHT *n* = 5 F, *n* = 5 M). Data are mean ± s.d. for image quantification and mean ± s.e.m. for flow cytometry data; two-way ANOVA with Tukey's test. Scale bars, 40 μm. F, female; M, male.

OBL cells and a decline in adipocytes in bones of 10.5-dpc pregnant dams compared to littermate virgins, males and other pregnant stages (Fig. 1a and Extended Data Fig. 1a,b). Increased percentage of total CD31⁺CD45⁻Ter119⁻ endothelial cells (ECs), CD31^high/Emcn^high (type-H) ECs within total ECs and proliferating (Ki-67⁺) ECs confirmed the promotion of angiogenesis on 10.5 dpc (Fig. 1b, Extended Data Fig. 1c and Supplementary Fig. 1).

To understand cellular changes in BMs during menopause, we generated a menopause mouse model by injecting vinylcyclohexene diepoxide (VCD) in 12-week-old females. Injection of VCD for 20 days and analysis after 32 days confirmed complete depletion of ovarian follicles (Supplementary Fig. 2), which modeled human menopause conditions[11,12]. Bones of menopause mice showed diminished total and type-H BECs (Fig. 1c) in addition to reduced OBL cells and increased adipocytes (Extended Data Fig. 1d). These findings show that pregnancy and menopause triggered significant changes in endothelial and mesenchymal compartments within the BM.

Estrogen regulates the growth of blood vessels in the bone

To understand the contribution of sex hormones in these cellular changes, we administered the sex hormones estradiol (E2; 17β-estradiol, 2 μg per day), progesterone (P4; 1 μg per day) and dihydrotestosterone (DHT; 100 μg per day) to young male and female mice for 10 days and analyzed their BMs after 2 weeks. Systemic treatment with E2 resulted in the accumulation of type-H capillaries in the bone marrow compartment. We observed a higher frequency of total and type-H ECs in bones of both sexes compared to P4-administered and DHT-administered bones (Fig. 1d and Extended Data Fig. 1e). Increase in OBL cells and decline in adipocytes of E2-treated bones indicated that cellular changes were similar to pregnancy-associated changes. Although OBL cells showed a marginal increase in DHT treatment, adipocytes were unaltered in both P4 and DHT treatments (Extended Data Fig. 2a). In addition to type-H capillaries, E2 promoted arteriolar (CD31⁺Emcn⁻ vessels) and transcortical vessels (TCVs) in E2-treated bones. Capillary subtypes were unaltered in P4 and DHT treatments (Extended Data Fig. 2b). Analysis of EC proliferation using 5-ethynyl-2′-deoxyuridine (EdU) labeling and Ki-67 immunostaining showed increased incorporation of EdU and frequency of Ki-67⁺ ECs in E2-treated bones. Likewise, cultured primary BECs showed increased proliferation in vitro upon E2 treatment (10 μM) (Extended Data Fig. 2c,d). We also analyzed transcript levels of angiogenic factors in purified BECs to understand angiogenesis. Higher expression of known angiogenic regulators in E2-treated BECs compared to vehicle controls supported the promotion of angiogenesis

in bones by elevated E2 levels (Extended Data Fig. 2e). Quantification of E2 levels at different stages of pregnancy (Extended Data Fig. 3a) confirmed elevated endogenous estrogen levels on 10.5-dpc pregnant dams corresponding with the status of angiogenesis in their bones. Similarly, aging reduced circulating E2 levels in mice (Extended Data Fig. 3b). To study blood vessel changes in bones under systemic low E2 conditions, we used ovariectomized (OVX) mouse models. Ovariectomy has been an established method to reduce circulating E2 levels and promote bone loss[13]. Ovariectomy was performed in 8-week-old female mice, and bones were analyzed after 6 weeks. OVX mice demonstrated vascular and mesenchymal phenotypes similar to ovarian follicle depletion. Recovery of bone phenotypes in OVX mice upon E2 administration established the central role of estrogen in this phenotype (Extended Data Fig. 3c). We also used the pharmacological aromatase inhibitor letrozole to arrest estrogen synthesis and, thus, reduce circulating E2 levels. Administration of letrozole (100 μg per day) in mice reduced angiogenic type-H capillaries and OBL cells and increased adipocytes in developing bones (Extended Data Fig. 3d). These findings established the role of estrogen in regulating the growth of blood vessels in the bone.

ER signaling in BECs

To study endothelial-specific changes mediated by estrogen, we investigated ER signaling in BECs. Transcript analysis for ERs in freshly isolated BECs showed expression of *Esr1* (ERα), *Esr2* (ERβ) and *Gper1* (GPER1) in both the sexes (Extended Data Fig. 4a). We investigated the functions of ERs in blood vessel growth by targeting individual receptors in BECs. We generated inducible EC-specific loss-of-function mice using loxP-flanked *Esr1* (*Esr1*^lox/lox)[14], *Esr2* (*Esr2*^lox/lox)[15] or *Gper1*(*Gper1*^lox/lox)[16] alleles with *Cdh5(PAC)-CreERT2* mouse line[17]. We analyzed postnatal (4-week-old) male and female bones to understand blood vessel changes. Gene deletions were confirmed by quantification of receptor transcript levels in purified BECs from control and mutant mice (Extended Data Fig. 4b). Deletion of one receptor showed minimal influence on the other receptors' transcript levels in BECs (Extended Data Fig. 4b). EC-specific loss of functions of *Esr1* and *Gper1* resulted in the reduction of total and type-H ECs, whereas *Esr2* mutants did not manifest endothelial phenotype in both sexes (Fig. 2). Thus, inhibition of ERs *Esr1* and *Gper1* impaired blood vessel growth in bones. We also observed a reduction of OBL numbers and an increase of adipocytes in *Esr1* and *Gper1* mutants (Extended Data Fig. 4c). We performed micro-computed tomography (micro-CT) analysis of *Esr1* and *Gper1* mutant bones to understand the changes at the whole organ level. Micro-CT data confirmed the reduction in trabecular bone and increase in lipid contents of both endothelial mutants (Extended Data Fig. 5a,b). Further analysis showed unaltered cortical bone thickness and area in these endothelial mutants. Similarly, osteoclasts on bone surfaces were not altered by the deletion of ERs on ECs. Vessel-associated osteoclasts, a subtype of osteoclasts present at the osteochondral interface, are dependent on angiogenic blood vessels[18]. The reduction of vessel-associated osteoclasts[18] in the metaphysis supported the defective blood vessel growth in these mutants (Extended Data Fig. 5a,b). These findings demonstrated the functional role of ER signaling in BECs and changes in the BM.

Metabolic regulation of BECs

Estrogen-mediated changes in the BM and similar endothelial ER mutant phenotypes in both female and male mice intrigued us to investigate sex differences in BECs. We performed RNA sequencing (RNA-seq) analysis for purified BECs of 2-, 12- and 65-week-old female and male mice to understand their sex differences. Gene expression analysis at different stages of growth and aging would provide age-related changes in endothelial sex differences. Principal component analysis (PCA) separated male and female ECs into two clusters, indicating variation between sexes at all age groups (Fig. 3a and Supplementary Dataset 1). The sex differences in BEC transcriptomes increased by age, with

48 differentially expressed (DE) genes in 2-week-old mice compared to 212 and 926 in 12- and 65-week-old mice, respectively, at $P_{adj} < 0.01$ significance level (Fig. 3b). We observed a strikingly low overlap in DE genes between the age groups, with the highest overlap of 72 genes detected between adult and aged mice (Fig. 3c and Extended Data Fig. 6a). To understand the significance of the gene expression data, we performed generally applicable gene set enrichment (GAGE) for pathway analysis for DE genes of 65-week data[19]. A total of four gene sets displayed significant levels of differences with a conspicuous enrichment of metabolic pathways gene set (Fig. 3d). Analysis of DE genes ($P_{adj} < 0.05$) in this metabolic pathways gene set showed a total of 142 genes altered between male and female BECs, with 43 genes being associated with FA metabolism (Extended Data Fig. 6b and Supplementary Dataset 1). However, there is limited understanding of the metabolism of BECs and their role in angiogenesis.

To understand the basal metabolic regulation of BECs, we tested major metabolic pathways that are known to regulate angiogenesis in other systems[20–22]. We checked for the nutrient supplements that could support the cultured BECs in the absence of FAs (serum-free), glucose and glutamine. We found that supplementation of primary BECs with FAs but not glucose or glutamine sustained BECs in vitro (Fig. 3e). The result prompted us to further investigate and inhibit FA metabolism in BECs. CPT1A, carnitine palmitoyltransferase 1a, is a rate-limiting enzyme of FA oxidation by transporting FAs into mitochondria. Treatment with the CPT1A inhibitor etomoxir reduced the growth of cultured BECs (Fig. 3f). Similarly, administration of etomoxir in postnatal day 10 (P10) mice for 10 days reduced the growth of blood vessels in bones (Fig. 3g). To investigate the bone endothelial-specific role of FA metabolism, we genetically targeted CPT1A in ECs using *Cpt1a floxed* mice[21] bred with EC-specific *Cdh5(PAC)CreERT2*. Loss of CPT1A function in BECs showed reduced oxidation of radiolabeled ³H-palmitate, indicating impaired FA metabolism (Fig. 4a). Analysis of blood vessels showed a reduction in total and type-H ECs of *Cpt1a*^iΔEC bones compared to their littermate controls, indicating defective blood vessel growth (Fig. 4a). In addition, *Cpt1a*^iΔEC mutant bones showed reduced OBL cells and increased adipocytes. Micro-CT analysis of mutant bones confirmed the changes in bone and lipid contents (Extended Data Fig. 6c), suggesting the importance of endothelial FA metabolism in regulating the BM.

We next investigated how estrogen influenced endothelial metabolism by treating primary BECs with E2. E2 did not alter the FA dependency of BECs in nutrient-depleted conditions (Fig. 3e). Furthermore, increased oxidation of ³H-palmitate compared to unaltered oxidation of ¹⁴C-glucose or ¹⁴C-glutamine suggested that E2 treatment promoted the use of FAs (Fig. 4b). Notably, etomoxir inhibited the E2-mediated cellular proliferation (Fig. 3f) and FA oxidation (Fig. 4c). To understand in vivo relation, we administered E2 in *Cpt1a*^iΔEC mutant mice to investigate angiogenesis. Administration of E2 did not recover angiogenesis inhibited in *Cpt1a*^iΔEC mutant bones, supporting the downstream FA dependency of E2-mediated blood vessel growth (Fig. 4d), whereas E2 increased OBL cells and reduced adipocytes in the mesenchymal compartment (Extended Data Fig. 6d). Together, the data indicated that estrogen required FAs to drive angiogenesis in bones.

Estrogen promotes FA uptake in BECs

Bone marrow adipocytes were suggested to release free FAs as an energy source for hematopoietic cells[23]. We identified that BECs expressed fatty acid binding protein 4 (FABP4), a membrane lipid transporter involved in FA uptake, transport and metabolism (Fig. 5a). E2-treated bones showed upregulation of FABP4 expression in their blood vessels (Fig. 5b and Extended Data Fig. 7a), which led us to investigate lipid transport in BECs. To analyze FA uptake in BECs, we provided a short 30-minute pulse of BODIPY-conjugated synthetic FAs in the medium. Detection of high BODIPY levels in E2-treated BECs compared to controls indicated the promotion of FA uptake by E2 (Fig. 5c and Extended
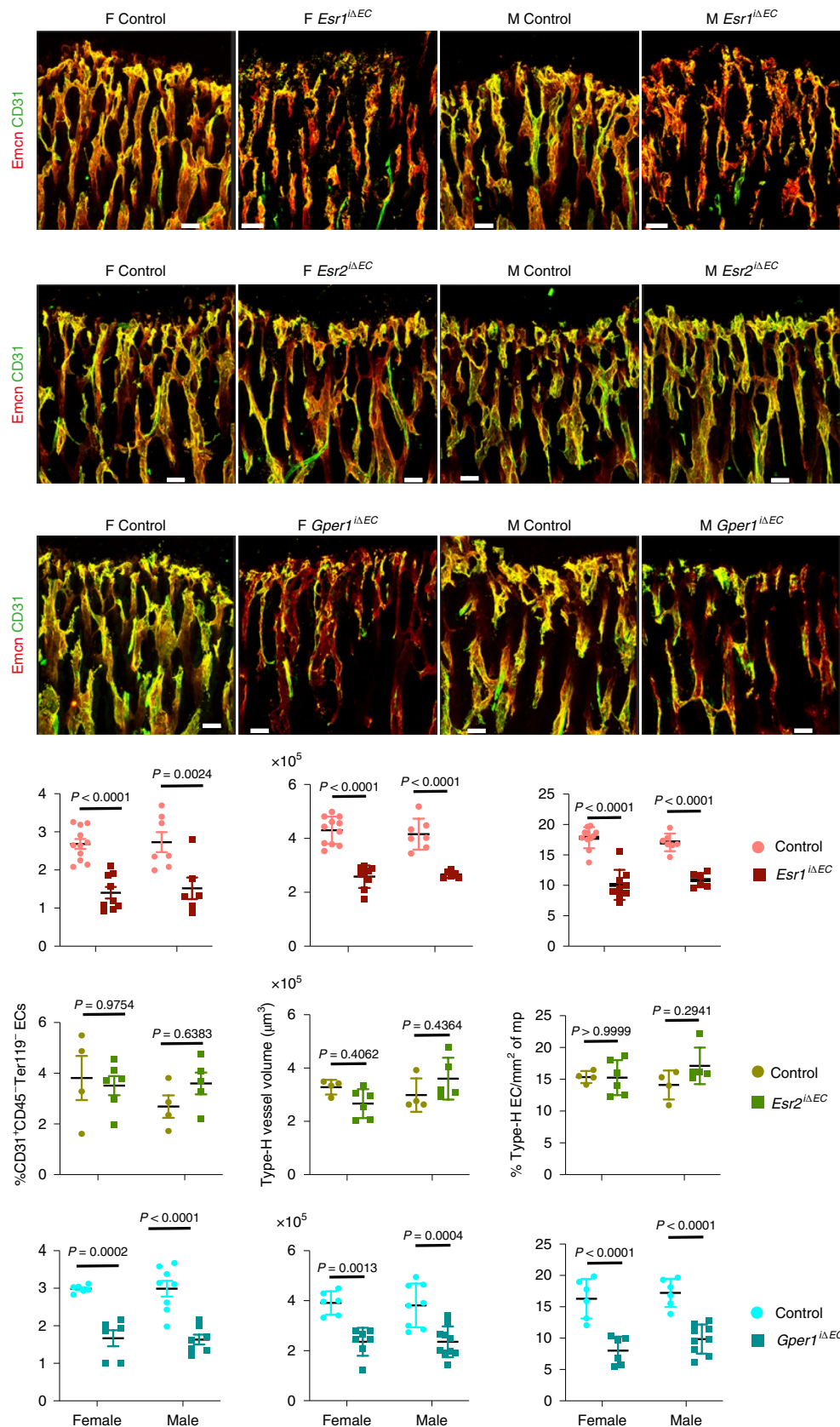
Fig. 2 | Estrogen signaling is mediated via ESR1 and GPER1. Representative confocal images of type-H (Emcn^high/CD31^high) vessel changes upon endothelial-specific deletion of ERs (*Esr1*, *Esr2* and *Gper1*) at P28 in mice. Graphs indicate quantifications of total ECs (CD31⁺CD45⁻Ter119⁻) by flow cytometry for *Esr1* (control n = 11 F, n = 7 M; mutant n = 9 F, n = 6 M), *Esr2* (control n = 4 F, n = 4 M; mutant n = 6 F, n = 5 M), *Gper1* (control n = 6 F, n = 8 M; mutant n = 6 F, n = 7 M); quantification of type-H vessel volume per field of mp for *Esr1* (control n = 11 F, n = 7 M; mutant n = 9 F, n = 6 M), *Esr2* (control n = 4 F, n = 4 M; mutant n = 6 F, n = 5 M), *Gper1* (control n = 6 F, n = 8 M; mutant n = 7 F, n = 10 M); and quantification of type-H EC area normalized to mp area for *Esr1* (control n = 11 F, n = 7 M; mutant n = 9 F, n = 6 M), *Esr2* (control n = 4 F, n = 4 M; mutant n = 6 F, n = 5 M), *Gper1* (control n = 6 F, n = 6 M; mutant n = 6 F, n = 9 M). Data are mean ± s.d. for image quantification and mean ± s.e.m. for flow cytometry data; two-way ANOVA with Tukey's test. Scale bars, 40 μm. F, female; M, male; mp, metaphysis.
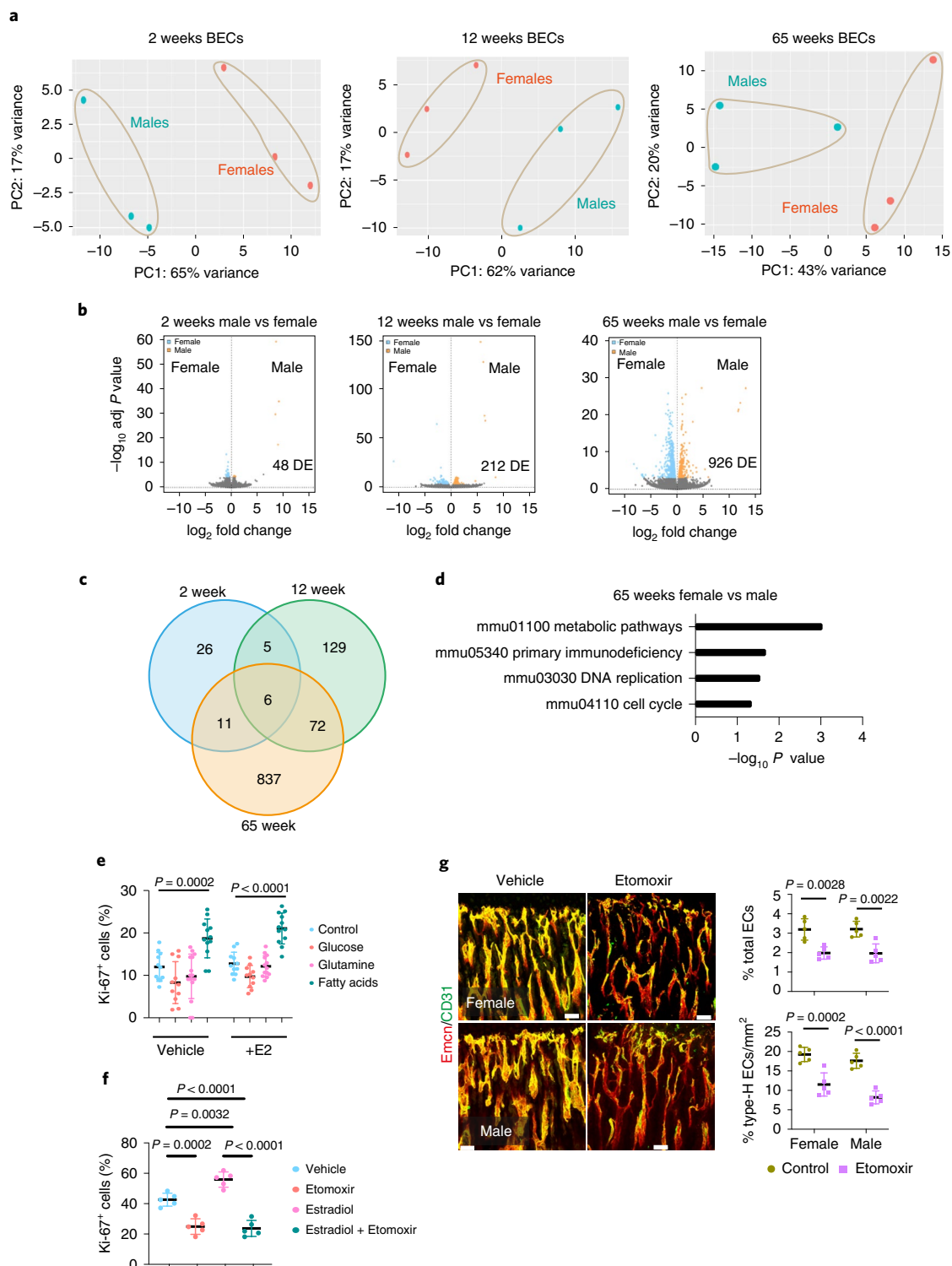
Fig. 3 | Metabolic regulation of BECs. a, PCA plots of RNA-seq data showing clustering by sexes in BECs from 2-, 12- and 65-week-old mice ($n = 3$). **b**, Volcano plots show the number of significant FDR-corrected (Bonferroni) P value ($P_{adj} < 0.01$) DE genes versus $\log_2$ fold change between female and male bone ECs of 2-, 12- and 65-week-old mice. DE genes were obtained by fitting each gene to a generalized linear model, followed by hypothesis testing using the Wald test. **c**, Venn diagram showing the overlap in DE genes between males and female bone ECs of 2-, 12- and 65-week-old mice. **d**, GAGE for pathway analysis for DE genes in RNA-seq data showing biological processes that differ between aged male and female BECs. Gene datasets of metabolic pathways, cell cycle and DNA are upregulated, and primary immunodeficiency pathway genes are downregulated. The significance of enrichment was calculated using two-sample t-tests, and the significant KEGG terms were selected using $P < 0.05$. **e**, Graph showing quantification of Ki-67$^+$-cultured BECs in the nutrient-free medium supplemented with glucose, glutamine or FAs, with vehicle (control $n = 9$, glucose $n = 11$, glutamine $n = 15$, FAs $n = 12$) and E2 treatment (control $n = 11$, glucose $n = 11$, glutamine $n = 13$, FAs $n = 12$). Data are mean ± s.d; two-way ANOVA with Tukey's test. **f**, Graph showing quantification of Ki-67$^+$-cultured BECs treated with vehicle or E2, with or without etomoxir treatment ($n = 5$). Data are mean ± s.d; two-way ANOVA with Tukey's test. **g**, Representative confocal images of type-H (Emcn^{high}/CD31^{high}) vessels in vehicle-treated and etomoxir-treated mice; quantification of type-H ECs normalized to the area of the metaphysis (mp) ($n = 5$). Data are mean ± s.d.; unpaired two-tailed t-test. Total ECs (CD31$^+$CD45$^-$Ter119$^-$) quantified by flow cytometry ($n = 5$). Data are mean ± s.e.m.; unpaired two-tailed t-test. Scale bars, 50 μm. PC, principal component.
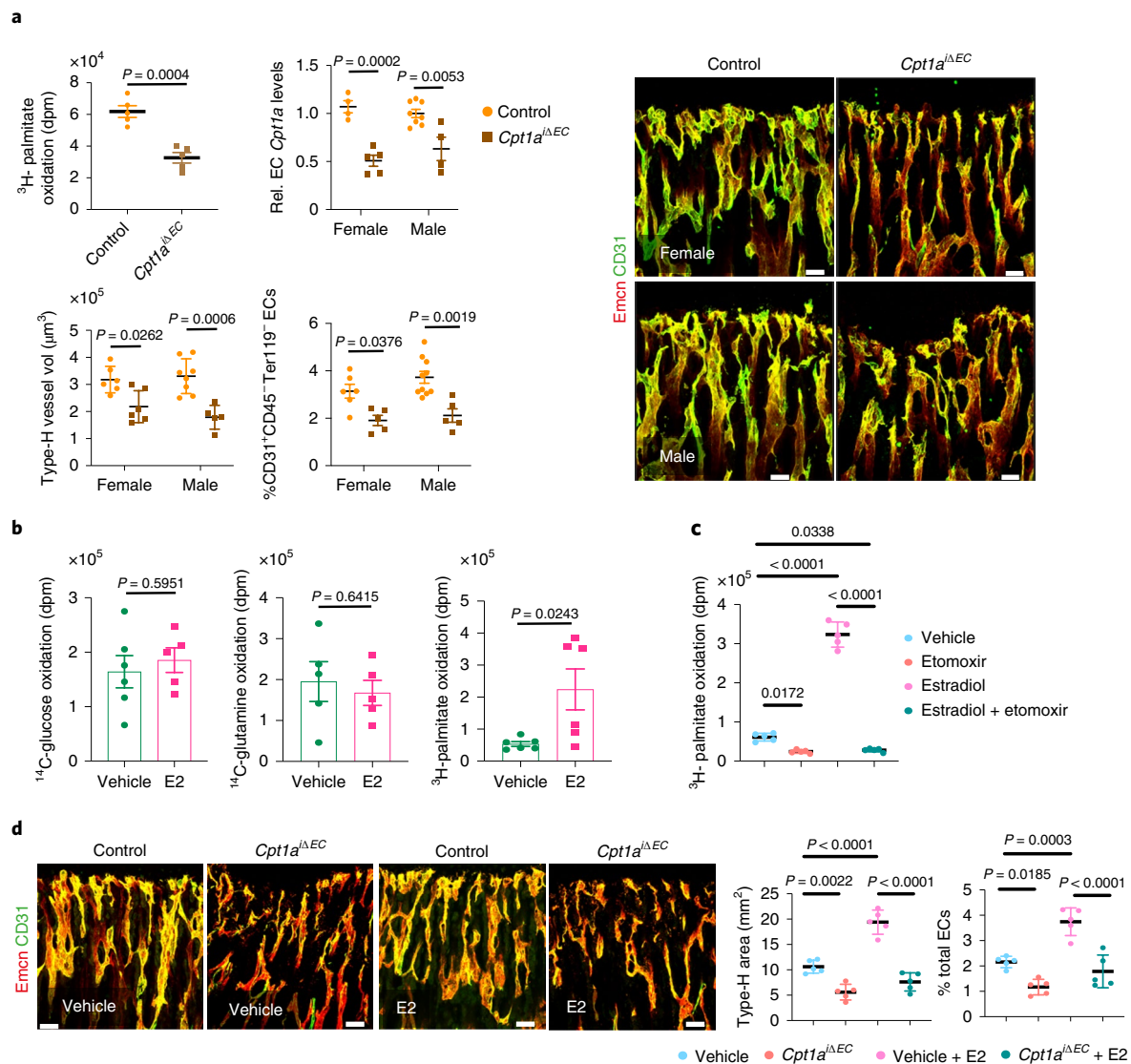
Fig. 4 | Estrogen-mediated bone endothelial growth is supported by FAs. a, Graph showing oxidation of ^{3}H-labeled palmitate by control and $Cpt1a$-deleted BECs. Graph shows $Cpt1a$ mRNA levels in purified BECs from control and $Cpt1a$ $^{i\Delta EC}$ mutant bones. Representative confocal images of type-H (Emcn^{high}/CD31^{high}) vessels in control and endothelial $Cpt1a$ deletion mutants, with quantification of type-H blood vessel volume (control n = 6 F, n = 8 M; mutant n = 6 F, n = 5 M) and total ECs (CD31$^+$CD45$^-$Ter119$^-$) characterized by flow cytometry (control n = 6 F, n = 5 M; mutant n = 10 F, n = 5 M). Data are mean ± s.d. for image quantification (type-H volume) and mean ± s.e.m for ^{3}H-palmitate, flow cytometry and qPCR data; two-way ANOVA with Tukey's test performed except ^{3}H-palmitate data (unpaired two-tailed t-test). Scale bars, 40 μm. **b**, Graphs showing glucose (vehicle n = 6, E2 n = 5), glutamine (vehicle n = 5, E2 n = 5) and palmitate (vehicle n = 6, E2 n = 6) oxidation in vehicle-treated and E2-treated BECs, measured by radioactivity (disintegrations per minute (dpm)). Data are mean ± s.e.m.; unpaired two-tailed t-test. **c**, Graph showing palmitate oxidation by BECs treated with vehicle or E2, with or without etomoxir treatment (n = 5). Data are mean ± s.e.m; two-way ANOVA with Tukey's test. **d**, Representative confocal images depicting type-H (Emcn^{high}/CD31^{high}) vessels in control and $Cpt1a$ $^{i\Delta EC}$ mutant mice treated with E2. Scale bars, 50 μm. Quantifications show type-H ECs normalized to the area of mp (control n = 5 F, n = 5 M; mutant n = 5 F, n = 5 M) and total ECs (CD31$^+$CD45$^-$Ter119$^-$) quantified by flow cytometry (control n = 5 F, n = 5 M; mutant n = 5 F, n = 5 M). Data are mean ± s.d. for image quantification and mean ± s.e.m for flow cytometry data; two-way ANOVA with Tukey's test. F, female; M, male; mp, metaphysis.

Data Fig. 7b). We also checked FA levels in BECs after E2 treatment using LipidTOX. Detection of more BECs with high intracellular lipid levels supported lipid uptake upon E2 treatment (Extended Data Fig. 7c). To understand the functional role of FABP4 in FA uptake, we treated BECs with the pharmacological FABP4 inhibitor BMS-309403 in the presence and absence of E2. Reduced BODIPY levels in BECs treated with BMS-309403 (Fig. 5c) indicated the involvement of FABP4 in E2-mediated FA uptake. Furthermore, we investigated lipid uptake in the presence of the ER signaling inhibitor G36, a pharmacological antagonist of GPER1. Impaired BODIPY uptake in BECs treated with G36 confirmed lipid transport as a downstream mechanism of ER signaling (Extended

Data Fig. 7d). In addition, reduced FABP4 expression in blood vessels of $Esr1$ $^{i\Delta EC}$ and $Gper1$ $^{i\Delta EC}$ mutant mice (Extended Data Fig. 7e) indicated the association between defective FA uptake and reduced angiogenesis.

Metabolic coupling of BECs and adipocytes

Defective FA uptake and angiogenesis in BECs of $Esr1$ $^{i\Delta EC}$ and $Gper1$ $^{i\Delta EC}$ mutant bones were associated with the accumulation of adipocytes in the microenvironment. Age-related decline in angiogenesis and osteogenesis[6,7,9,24,25] involved a concurrent increase in adipocytes[26,27]. Reduced angiogenic status of aging bones is associated with an increase in the number and size of adipocytes in the BM. On the contrary, young

bones with high angiogenesis showed smaller and fewer adipocytes, indicating an inverse relationship between angiogenic ECs and adipocytes (Fig. 5d,e). Smaller adipocytes present in young bones showed high expression of the lipolytic enzymes adipose triglyceride lipase (ATGL) and hormone-sensitive lipase (HSL) compared to larger adipocytes present in aged bones. Thus, limited adipocytes present in young angiogenic bones displayed high levels of lipolytic enzymes. Likewise, aged bones with reduced angiogenesis showed low levels of lipolytic lipases in their adipocytes (Fig. 5d,e).

Adipocytes have previously been shown to express ERs and respond to circulating estrogen levels[28,29]. However, variation of adipocyte numbers in endothelial mutants (see adipocyte phenotypes of *Esr1*[iΔEC], *Gper1*[iΔEC] and *Cpt1a*[iΔEC] mice) prompted us to investigate the expression of lipolytic enzymes in these mutants. Adipocytes present in *Cpt1a*[iΔEC] and *Gper1*[iΔEC] mutant bones showed low levels of lipolytic lipases (Extended Data Fig. 8a). The data indicated the involvement of BECs in regulating lipolysis of adipocytes in the BM. To identify potential EC-derived signals acting on adipocytes, isolated BECs were analyzed for the expression of lipolytic factors. Purified BECs from E2-administered mice showed upregulation of *Tnfa* and *Il6*, which are well-recognized paracrine lipolytic factors. Impaired ER signaling in *Esr1*[iΔEC] and *Gper1*[iΔEC] mutant BECs showed downregulation of endothelial *Tnfa* and *Il6* levels (Extended Data Fig. 8b). Reduced expression of these lipolytic factors supported the accumulation of adipocytes in these mutant bones. Likewise, E2 treatment of in vitro cultured BECs released higher levels of TNF-α and IL-6 in the medium compared to control treatment (Extended Data Fig. 8c), confirming their angiocrine release from BECs. Decreased angiogenesis and, thus, lipid use in BECs is associated with the reduced lipolysis and accumulation of adipocytes in the BM. These data suggest metabolic interaction between angiogenesis and lipolysis in the BM.

Accumulation of LPOs in aging BECs

Skeletal aging is associated with changes in blood vessels that contribute to bone loss[9,24,25]. Age-related decline in estrogen levels[30–33] led to severe bone loss in females. Estrogen administration has been shown to prevent age-related bone loss[34–37]. Administration of E2 in aging mice promoted total ECs, type-H capillaries and OBL cells and decreased adipocytes (Extended Data Fig. 9a). We also noted an increase in arterioles and transcortical vessels in the bones of E2-administered mice (Extended Data Fig. 9b). Age-associated increase in cellular reactive oxygen species (ROS)[38] has been widely recognized. Remarkably, E2 administration in aging mice significantly reduced endothelial ROS levels in blood vessels (Fig. 6a). Further analysis showed accumulation of LPOs in aging BECs as evidenced using 4-hydroxynonenal[39] (HNE) levels and BODIPY 665/676, an LPO sensor. We found reduced LPO levels in BECs of E2-administered mice (Fig. 6b,c and Extended Data Fig. 9c). Likewise, an increase in endothelial HNE of menopause-induced bones argued for the high lipid peroxidation in estrogen-depleted conditions (Extended Data Fig. 9d).

FABP4 has been shown to contribute to protection against oxidative stress by reducing cellular ROS[40]. Notably, E2 administration improved FABP4 expression in aged bone endothelium and indicated a potential relation between FABP4 and LPOs in BECs (Extended Data Fig. 10a). Inhibition of FABP4 in BECs showed accumulation of HNE, suggesting its involvement in LPO generation (Extended Data Fig. 10b). E2 supplementation could not reduce FABP4-mediated HNE accumulation, indicating FABP4 dependency of E2 function (Extended Data Fig. 10b). In addition, the data argued for investigating E2 function in the regulation of multiple cellular mechanisms that result in the generation of peroxides.

Aging of bone ECs

Cellular Fe^{2+} levels contribute to the generation of LPOs in cells through a ferroptosis-dependent mechanism[41,42]. To understand the contribution of Fe^{2+} in age-related increase in endothelial LPO levels, we investigated Fe^{2+} concentration in both male and female BECs. Intracellular labile Fe^{2+} concentration was higher in purified male BECs compared to females and was unaltered by E2 treatment in young BECs (Fig. 6d). We then used FeRhoNox-1 labeling to detect and quantify Fe^{2+} levels in BECs. FeRhoNox-1 labeling also detected high Fe^{2+} levels in young male BECs compared to females. Interestingly, quantification in aged bones showed a higher percentage of Fe^{2+} BECs in aging females compared to males (Fig. 6e). Culturing of primary BECs with deferoxamine mesylate (DFM), an iron chelator, resulted in the reduction of endothelial LPO levels. Correspondingly, induction of Fe^{2+}-mediated peroxide production using artemisinin increased endothelial LPO levels. E2 treatment reduced LPO levels in both DFM-treated and artemisinin-treated BECs in vitro (Extended Data Fig. 10c). DFM has been shown to promote type-H vessels and osteogenesis in aged mice[9]. We found reduced LPO levels in BECs of mice administered with DFM (Extended Data Fig. 10d). Likewise, treatment of artemisinin (200 mg kg^{-1}) in young mice led to a reduction in type-H capillaries and OBL cells with no change in adipocytes (Extended Data Fig. 10e). These data suggested the role of Fe^{2+} in endothelial LPO production and, thus, aging phenotype of blood vessels in the bone.

High basal Fe^{2+} levels in aged female ECs could aggravate LPO production and loss of type-H and bone in estrogen-depleted conditions such as menopause. The reduction of LPO production by E2 (Fig. 6b,c) suggested a potential mechanism underlying the clinical benefits of hormone replacement therapy (HRT) for postmenopausal bone loss. To test this, we pharmacologically targeted LPO production using liproxstatin-1 (Lip-1), a lipid peroxide inhibitor, in aged mice. Aged mice treated with vehicle control contained few type-H vessels compared to mice administered Lip-1 (10 mg kg^{-1}), which showed an increase in angiogenic capillaries (Fig. 6f). Analysis of ROS levels in BECs demonstrated a reduction in Lip-1-treated bones (Fig. 6g). Furthermore, Lip-1-mediated increase in type-H capillaries is associated with the increase in OBL cells and reduction in adipocytes in aged bones (Fig. 7a). Micro-CT analysis of aged bones confirmed the increase observed in bone and the reduction in lipid contents of Lip-1-treated mice (Fig. 7b and Extended Data Fig. 10f).

Fig. 5 | Estrogen regulation of endothelial lipid transport. a, Maximum intensity projection of confocal image showing overlap of FABP4 (green) expression in bone ECs overlap with the Emcn (red) expression. Scale bars, 50 μm. **b,** Graphs show quantification of FABP4 protein levels observed in bone tissue sections of vehicle-treated and E2-treated treated bones (*n* = 5) imaged using confocal microscopy. Data are mean ± s.d.; two-way ANOVA with Tukey's test. Transcript levels were quantified from isolated bone ECs of vehicle-administered and E2-administered mice (*n* = 5) using qPCR. Data are mean ± s.e.m.; two-way ANOVA with Tukey's test. **c,** Representative confocal images of lipid uptake of BODIPY-conjugated synthetic FAs in vehicle-treated and E2-treated BECs upon FABP4 inhibitor BMS-309403 treatment. Scale bars, 15 μm. Quantification shows reduced fluorescence units (FU, intensity) of endothelial BODIPY upon FABP4 inhibition across multiple ×63 fields of view (vehicle *n* = 37;

vehicle + BMS-309403 *n* = 36; E2 *n* = 41; E2 + BMS-309403 *n* = 42). Data are mean ± s.d.; two-way ANOVA with Tukey's test. **d,** Representative confocal images of BM adipocytes (perilipin$^+$, green) from young and aged bones. Scale bars, 50 μm. Graphs show average perilipin$^+$ adipocytes number (*n* = 17), size (*n* = 15) and fluorescence intensity quantification, indicating a decrease in the lipolytic enzyme ATGL in aged mice (*n* = 84 F, 52 M) compared to young mice (*n* = 50 F, 58 M) per cell across multiple ×20 fields of view. Data are mean ± s.d.; two-way ANOVA with Tukey's test. **e,** Representative confocal images of BM adipocytes (perilipin$^+$), with fluorescence intensity quantification indicating a decrease in the lipolytic enzyme HSL in aged mice (HSL *n* = 120 F, 168 M) compared to P28 mice (HSL *n* = 78 F, 88 M) per cell across multiple ×20 fields of view. Data are mean ± s.d.; two-way ANOVA with Tukey's test. Scale bars, 50 μm. F, female; M, male; Plin, perilipin.

Discussion

In this study, we found that estrogen plays an important role in mediating blood vessel growth by promoting FA metabolism in BECs (Fig. 8). Genetic ER loss-of-function studies indicate constituent estrogen signaling in bone vasculature of both male and female BECs and strongly

argue for investigating their dose-dependency, interactions and redundancy in mediating downstream signaling.

Angiogenesis in actively growing bones is linked with limited adipocyte number, and the age-related decline in angiogenesis is associated with the accumulation of adipocytes in the bone. In women,
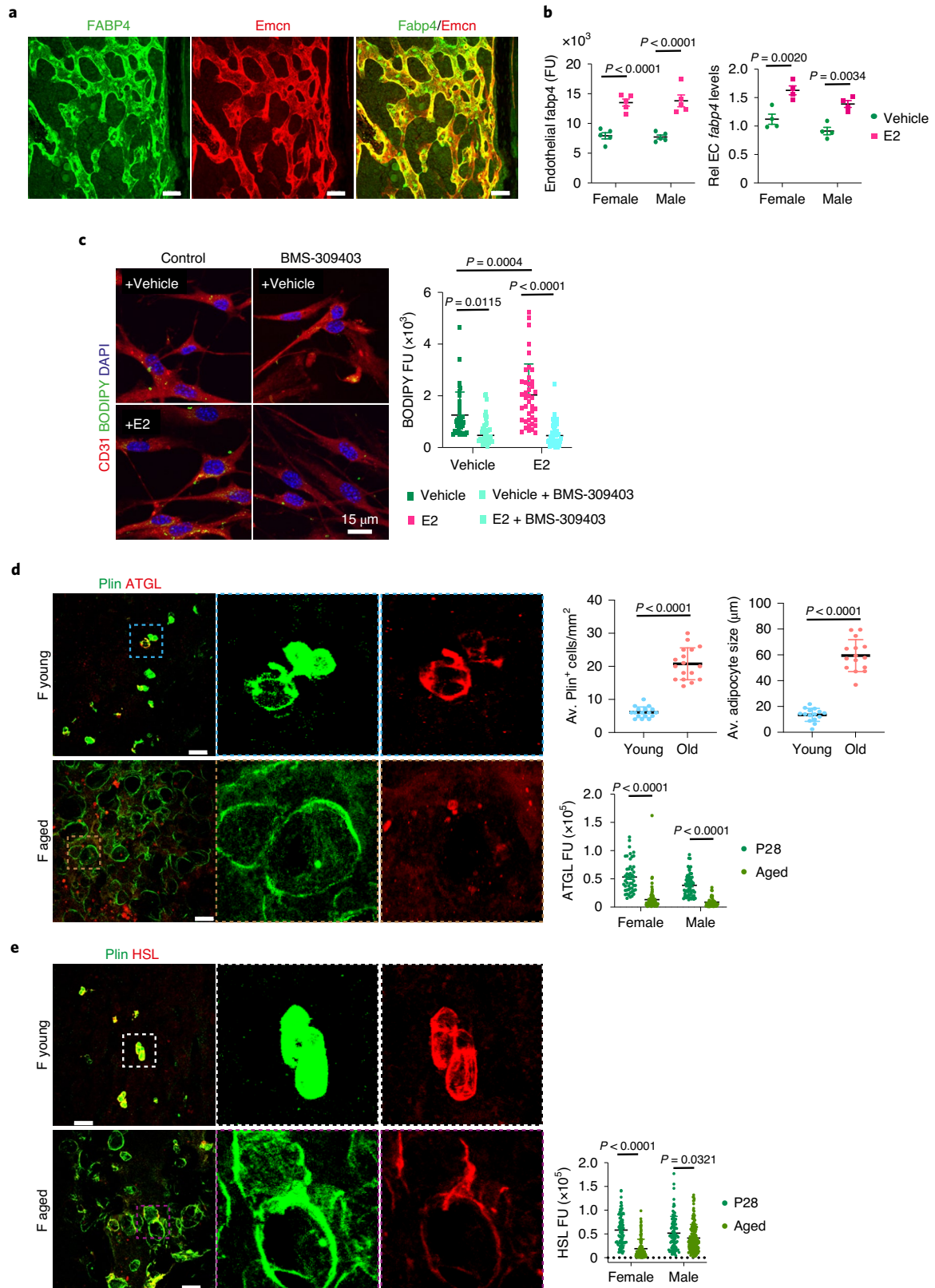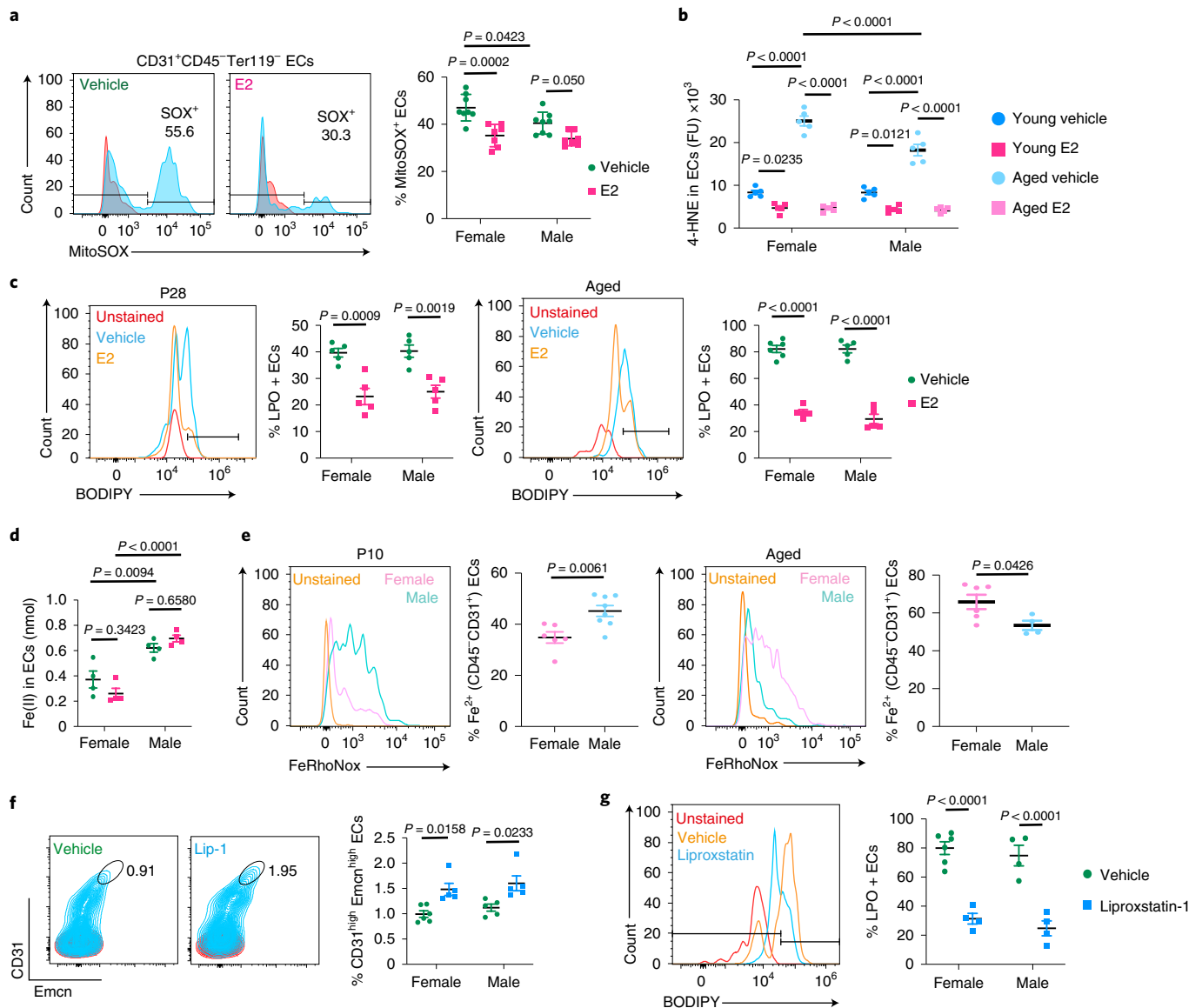
Fig. 6 | Defective lipid metabolism promotes vascular aging in bones. a, Representative flow cytometry plots of ROS generation in ECs from vehicle-treated mice (n = 8 F, n = 8 M) and E2-treated mice (n = 7 F, n = 7 M). Red peaks in the histogram plots indicate unstained cells. Quantifications show a reduction in ROS upon E2 treatment. Data are mean ± s.e.m.; two-way ANOVA with Tukey's test. **b**, Quantifications of 4-HNE levels in ECs from immunostaining in young vehicle-treated mice (n = 5 F, n = 5 M) and E2-treated mice (n = 5 F, n = 5 M) and aged vehicle-treated mice (n = 5 F, n = 5 M) and E2-treated mice (n = 5 F, n = 5 M), showing a reduction in 4-HNE levels upon E2 treatment. Data are mean ± s.d.; two-way ANOVA with Tukey's test. **c**, Representative flow cytometry plots of LPO generation in ECs from young vehicle-treated mice (n = 5 F, n = 5 M) and E2-treated mice (n = 5 F, n = 5 M) and aged vehicle-treated mice (n = 6 F, n = 5 M) and E2-treated mice (n = 5 F, n = 5 M). Red peaks in the histogram plots indicate unstained cells. Quantifications show a reduction in LPO upon E2 treatment.

Data are mean ± s.e.m.; two-way ANOVA with Tukey's test. **d**, Graph showing sex differences in intracellular ferrous ion concentrations in BECs of vehicle-treated and E2-treated mice (n = 4). Data are mean ± s.e.m.; two-way ANOVA with Tukey's test. **e**, Representative flow cytometry plots with quantifications showing sex differences in intracellular ferrous ions in BECs at P10 mice (n = 6 F, n = 8 M) and aged mice (n = 6 F, n = 4 M). Data are mean ± s.e.m.; unpaired two-tailed t-test. **f**, Representative flow cytometry plots with quantifications showing increase in type-H ECs (CD31^high/Emcn^high) with Lip-1 treatment in aged mice (vehicle n = 6 F, n = 5 M; Lip-1 n = 5 F, n = 5 M). Data are mean ± s.e.m.; two-way ANOVA with Tukey's test. **g**, Representative flow cytometry plots of BEC populations of aged vehicle-treated and Lip-1-treated mice. Quantifications are of ECs with lipid ROS (vehicle n = 6 F, n = 4 M; Lip-1 n = 4 F, n = 4 M), indicating a reduction upon Lip-1 treatment. Red peaks in the histogram plots indicate unstained cells. Data are mean ± s.e.m.; two-way ANOVA with Tukey's test. F, female; M, male.

estrogen treatment has been identified to cause lipolysis and reduce bone marrow lipid content[43]. The role of estrogen in regulating bone adipocytes has been widely recognized. Here we show a previously unknown association between blood vessels and adipocytes. We found that inhibition of lipid metabolism in BECs led to increased adipocytes in the BM. In menopausal animal models, reduction of angiogenesis is associated with the accumulation of adipocytes, similar to aging in humans. Our data propose that estrogen could regulate metabolic

coupling to maintain energy balance in the BM by driving lipolysis for the growth of blood vessels.

The tissue-specific nature of vascular aging[44] is still in the initial stages of understanding. We found that intrinsic ferrous ion levels could accelerate the aging of BECs and contribute to bone loss observed in aging females compared to males. The iron-dependent, non-heme nature of lipoxygenases corroborates the importance of iron in endothelial LPO levels. Overall, estrogen is a key factor that limits LPO
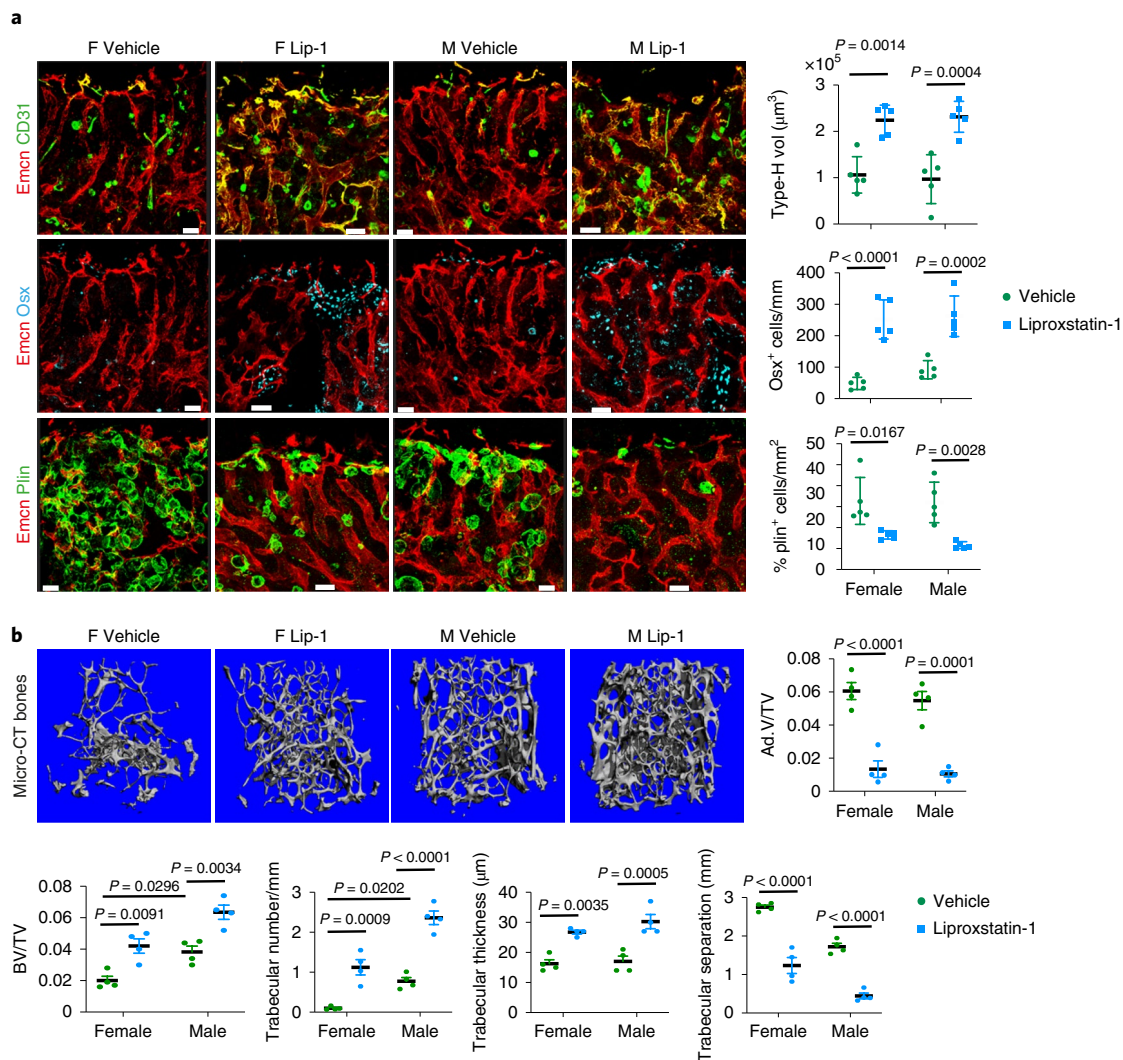
Fig. 7 | Lip-1 protects against age-related bone loss. a, Representative confocal images of BM in aged mice treated with Lip-1, with graphs showing quantification of type-H vessel volume per field of mp (vehicle $n = 5$ F, $n = 5$ M; Lip-1 $n = 5$ F, $n = 5$ M), osterix$^+$ cells per mm of mp (vehicle $n = 5$ F, $n = 5$ M; Lip-1 $n = 5$ F, $n = 5$ M) and perilipin$^+$ area per mm area (vehicle $n = 5$ F, $n = 5$ M; Lip-1 $n = 5$ F, $n = 5$ M). Data are mean ± s.d.; two-way ANOVA with Tukey's test. Scale bars, 40 μm (vehicle) and 50 μm (Lip-1). **b**, Representative micro-CT images of bones from aged mice treated with Lip-1, with graphs showing quantification of trabecular bone volume, number, thickness and separation ($n = 4$) and adipocyte volume ($n = 4$). Data are mean ± s.e.m.; two-way ANOVA with Tukey's test. F, female; M, male; Osx, osterix; Plin, perilipin.

accumulation in BECs. Combined effects of reduced estrogen, ferrous ions and LPOs contribute to accelerated aging in females. This study supports the fundamental notion of investigating sex differences in the vasculature to understand gender bias observed in the incidences of age-related cardiovascular diseases. Findings from this study identify LPOs as a downstream target of estrogen and suggest that targeting LPOs could be an alternative strategy to HRT to treat postmenopausal bone loss and bone repair. Moreover, the fundamental knowledge of bone endothelial sex differences can be beneficial in developing precision medicine against blood and bone diseases.

Methods

Mice

All animal experiments were carried out in accordance with institutional guidelines and laws, following the protocols approved by the Imperial College London Animal Welfare and Ethical Review Body and the Home Office UK. All wild-type experiments were performed in C57BL/6J mice and were age-matched and sex-matched. All transgenic mice were age-matched and sex-matched for each experiment.

For the pregnancy experiments, the onset of pregnancy was determined by the presence of a vaginal plug. Mice were culled on relevant days after identification of vaginal plug, along with virgin females and male mice as controls.

For hormonal treatments, mice were injected subcutaneously (s.c.) with 2 μg of 17β-estradiol (Acros Organics), 1 mg of progesterone (Acros Organics) or 100 μg of DHT (TCI) dissolved in ethanol and corn oil (100 μl). Vehicle mice received the equivalent dose of ethanol in corn oil. Pups (P10) were given ten intermittent injections, and aged mice (65–75 weeks) received three injections per week for 6 weeks. Mice injected with 17β-estradiol were injected intraperitoneally (i.p.) with EdU (250 mg ml^{-1}) 3 hours before culling to identify ECs undergoing proliferation. Pups (P10) received ten doses of 10 μg of letrozole (Sigma-Aldrich) in DMSO for anti-aromatase treatment.

For the murine menopause model, female mice were injected with 160 mg kg^{-1} day^{-1} of 4-vinyl cyclohexene diepoxide (Fluorochem) for 20 days and left for a further 32 days to induce complete follicular atresia. Vaginal samples were taken daily to confirm persistent dioestrus. Control mice were injected with PBS.
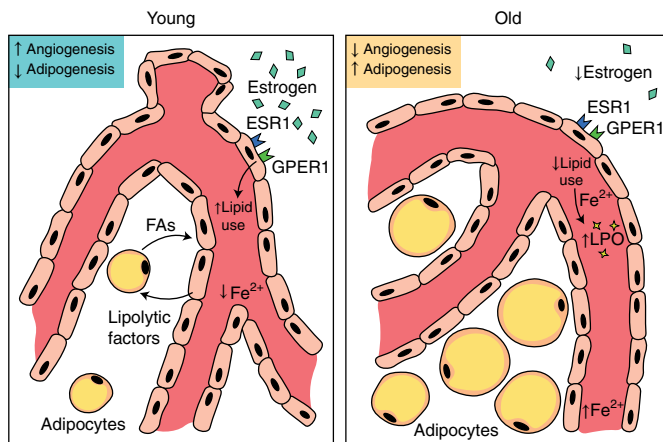
Fig. 8 | Schematic representation of key findings. Estrogen regulates the growth of blood vessels in bone through endothelial ESR1 and GPER1. ER signaling regulates ECs' use of FA metabolism by promoting angiocrine release of lipolytic factors, enzymes and FA uptake from the microenvironment. Impaired lipid metabolism in aged endothelium and sex differences in endothelial ferrous ion levels stimulate aging phenotype in blood vessels of bones.

OVX mice were purchased from Charles River Laboratories UK. Ovariectomy was performed on C57BL/6J wild-type mice. E2 cohorts received 17β-estradiol 2 weeks after the surgery for 4 weeks (three injections per week), whereas control cohorts received vehicle injections.

DFM was administered at 25 μg g^{-1} weight of mice i.p. for 2 weeks every alternate day. Mice were sacrificed the day after the last injection for analysis. To inhibit CPT1A, etomoxir at 30 mg kg^{-1} was injected i.p. for 10 days, and mice were sacrificed on P28.

For endothelial-specific deletion of ERs, conditional *Esr1$^{lox/lox}$*, *Esr2$^{lox/lox}$* or *Gper1$^{lox/lox}$* mice were bred with *Cdh5(PAC)-CreERT2* transgenic mice. Cre activity was induced by tamoxifen (80 mg kg^{-1}) injections from P10–P14 mice, and mice were analyzed at P28. Littermate Cre- mice were also injected with tamoxifen and used as controls. Similarly, conditional *Cpt1a$^{lox/lox}$* mice were bred with *Cdh5(PAC)-CreERT2* transgenic mice for endothelial-specific deletion, and mice were analyzed at P28. To induce Cre activity at the adult stage, mice were injected from P66 to P70 and culled on P84.

To induce the generation of LPOs in young mice, pups (P10) were given five intermittent i.p. injections of artemisinin (TCI, 200 mg kg^{-1}) in DMSO. Aged mice received 15 doses of Lip-1 (Tocris Bioscience, 10 mg kg^{-1}) i.p. for 4 weeks to inhibit LPO production.

Bone processing, immunohistochemistry and confocal microscopy
Tibiae were dissected and cleaned and underwent immediate fixation for 4 hours on ice in 4% paraformaldehyde (PFA) solution, followed by decalcification with 0.5 M EDTA with constant agitation at 4 °C. Bones were then kept in cryo-preservative solution (20% (w/v) sucrose and 2% (w/v) polyvinyl pyrrolidine (PVP)) for a further 48 hours. For cryosectioning, bones were embedded in 8% (w/v) gelatin, 20% (w/v) sucrose and 2% (w/v) PVP. A Leica cryostat was used to generate 70-μm sections on microscopic slides used for immunostaining.

For phenotypic analyses of tibiae by immunohistochemistry, bone sections were hydrated with PBS, followed by permeabilization with 0.25% Triton X-100 for 10 minutes and blocking with 5% donkey serum (DS) for 30 minutes. Primary antibody was diluted in 5% DS and incubated for 2.5 hours at room temperature or overnight at 4 °C. Primary antibodies used included anti-endomucin (Santa Cruz Biotechnology, 1:100), anti-osterix (Abcam, 1:600), anti-CD31 (R&D Systems, 1:100), anti-perilipin (Cell Signaling Technology, 1:100), anti-perilipin (GeneTex, 1:100), anti-Ki-67 (Abcam, 1:100), anti-laminin (Sigma-Aldrich,

1:100), anti-FABP4 (R&D Systems, 1:100), anti-4-hydroxynonenal (Abcam, 1:200), anti-HSL (Cell Signaling Technology, 1:50), anti-ATGL (Cell Signaling Technology, 1:100), anti-CD45 (BD Pharmingen, 1:100) and anti-Itgb3 (Cell Signaling Technology, 1:100).

Slides were then washed three times with PBS for 5 minutes each and incubated with fluorophore-conjugated secondary antibody diluted in 5% DS for 1 hour at room temperature. Secondary antibodies used included anti-rat Alexa Fluor 594 (Invitrogen, A21209, 1:400), anti-rat Alexa Fluor 488 (Invitrogen, A21208, 1:400), anti-goat Alexa Fluor 488 (Invitrogen, A11055, 1:400), anti-goat Alexa Fluor 546 (Invitrogen, A11056, 1:400), anti-goat Alexa Fluor 647 (Invitrogen, A21447; 1:400), anti-rabbit Alexa Fluor 488 (Invitrogen, A21206, 1:400), anti-rabbit Alexa Fluor 546 (Invitrogen, A10040, 1:400) and DAPI for nuclear staining. Slides were washed three times with PBS for 10 minutes each and then mounted with a coverslip using Fluoromount G solution (Southern Biotech).

EdU labeling was performed by Click-iT chemistry (Invitrogen, C10340) following the manufacturer's guidelines, after primary and secondary antibody incubations.

High-resolution three-dimensional (3D) images were acquired using a Leica TCS SP8 confocal laser scanning microscope using Leica LASX software.

Micro-CT analysis
We collected fresh tibiae and femur from mutants and their littermate controls or from control and treated mice for phenotype analysis using micro-CT. Freshly isolated bones were cleaned thoroughly and fixed in 4% PFA. For analyzing mineralized regions in bones, fixed bones were used for micro-CT scanning. For lipid analysis, we performed osmium tetroxide labeling. In brief, fixed bones were decalcified in EDTA solution for 3–10 days and stained with 2% osmium tetroxide solution for 48 hours. Bones were then washed thoroughly and stored until analysis. The bones were scanned using cabinet cone-beam micro-CT (μCT 100, Scanco Medical) and IPL software version 5.15 at Scanco Medical. A voxel size of 10 μm was chosen in all three spatial dimensions. For each sample, at least 400 slices were evaluated, covering more than 4 mm at a voltage of 70 kVp, intensity of 114 μA, 8 W and integration time of 800 ms. For evaluation, 3-mm length below the growth plate was chosen as the volume of interest.

Isolation and culture of primary murine BECs
Tibiae and femurs were dissected and collected in ice-cold PBS and washed subsequently with sterile PBS under sterile conditions. Bones were crushed with a mortar and pestle, and the remaining bone debris was digested with collagenase for 20 minutes at 37 °C and filtered together to obtain a single-cell suspension. Red blood cell (RBC) lysis (ChemCruz) was performed (5 minutes, room temperature) to eliminate RBCs, and then total cells were pelleted and kept on ice.

BECs were isolated using Dynabeads sheep anti-rat IgG (Invitrogen) following the manufacturer's protocol. In brief, beads were first coated with rat endomucin (Santa Cruz Biotechnology) for 45 minutes on a rotator at 4 °C, washed with isolation buffer (0.1% FBS-PBS) on a magnetic rack and then incubated with total cells for 30 minutes on a rotator at 4 °C to isolate ECs only. The mixture was washed with isolation buffer on a magnetic rack to isolate a positive selection of endomucin-expressing cells and plated in fibronectin-coated (Sigma-Aldrich) cell culture plates in EBM-2 basal medium (Lonza) supplemented with EGM-2 growth medium (2% FBS, 0.4% hFGF-B, 0.1% VEGF, 0.1% R3-IGF-1, 0.1% ascorbic acid, 0.1% hEGF, 0.1% heparin and 0.04% hydrocortisone). Cells were passaged every 3–4 days using 0.25% trypsin-EDTA (Sigma-Aldrich).

In vitro assays
Nutrient supplementation. BECs grown in EGM2 complete medium for 1 day were used for this experiment. After washing with HBSS, cells

were treated either with vehicle (DMSO) or with 17β-estradiol (10 μM) for 16 hours in glucose-free, glutamine-free and serum-free EC medium (Cell Biologics) and supplemented with 5 mM glucose, 2 mM glutamine or 20 mM linoleic acid–oleic acid (Sigma-Aldrich) to determine the effect of nutrient supplementation on cell growth. Cells were stained with anti-Ki-67 antibody (Abcam, 1:300) to measure EC proliferation or with anti-cleaved caspase-3 antibody (Cell Signaling Technology, 1:300) to measure apoptosis.

Lipid uptake. BECs cultured on coverslips were treated with vehicle (DMSO) or 17β-estradiol for 60 hours and then either incubated with BODIPY 558/568 C12 (Thermo Fisher Scientific, 1 μM) or stained with HCS LipidTOX Green (Thermo Fisher Scientific, 1:1,000) for 30 minutes at 37 °C. Cells were washed and mounted on slides and imaged using a Leica TCS SP8 confocal microscope.

CPT1A inhibition. BECs cultured on coverslips were treated with vehicle (DMSO) or 17β-estradiol along with etomoxir (100 μM). Cells were stained with anti-Ki-67 antibody (Abcam, 1:300) to measure EC proliferation or with anti-cleaved caspase-3 antibody (Cell Signaling Technology, 1:300) to measure apoptosis.

FABP4 inhibition. BECs cultured on coverslips were treated with vehicle (DMSO) or 17β-estradiol along with BMS-309403 (10 μM). Cells were stained with BODIPY 558/568 C12 to determine whether lipid uptake was reduced.

GPER1 signaling inhibition. BECs cultured on coverslips were treated with vehicle (DMSO) or 17β-estradiol along with G36 (Tocris Bioscience, 10 μM) for 60 hours and then stained for BODIPY 558/568 C12 as explained for lipid uptake.

Iron assay. BECs were cultured from male and female bones separately and treated with vehicle (DMSO) or 17β-estradiol for 60 hours before the assay. BECs were collected by trypsinization and centrifugation and lysed by sonication and resuspended in iron assay buffer (Abcam, ab8366.) The assay was performed as per manufacturer guidelines for the Iron (II) assay with optical density (OD) measured at 593 nm and Iron (II) content determined by a standard curve.

LPO assay. LPOs generated by ferrous ion redox reactions were measured by a colorimetric assay (Cayman Chemical, 705003) following the manufacturer's protocol. In brief, total ECs were isolated from the bones of young and aged mice treated with vehicle or E2 as explained previously using Dynabeads and lysed by sonication upon bead removal. A methanol: chloroform extraction followed, taking the chloroform layer for reaction with thiocyanate ions to detect LPOs generated by measuring OD at 500 nm using FLUOstar Omega Microplate reader 3.0.

17β-estradiol ELISA. The concentration of 17β-estradiol was determined from blood serum by an ELISA (Abcam, ab108667) according to the manufacturer's protocol. Circulating blood was collected from mice and allowed to clot for 45–60 minutes at room temperature and centrifuged at 3,500 r.p.m. for 10 minutes to obtain serum. The 17β-estradiol–HRP conjugate was added to samples or standards and incubated for 2 hours at 37 °C. After washing of all samples, TMB substrate was added and incubated for a further 30 minutes at room temperature. The reaction was halted by the addition of a stop solution, and OD was measured at 450 nm to quantify E2 concentration using a standard curve.

ELISA. Supernatant was collected from cultured BECs treated with vehicle (DMSO) or 17β-estradiol to measure the concentration of TNFα (R&D Systems, MTA00B) and IL-6 (R&D Systems, M6000B) released

using ELISA according to the manufacturer's protocol. Specifically, assay diluent was added to standards or samples and incubated for 2 hours at room tempterature. After washing of all samples, respective protein conjugate was added for 2 hours, followed by further washing and incubation with substrate solution for 30 minutes. OD was measured at 540 nm and 450 nm (subtracted for wavelength correction), and protein concentrations were determined by a standard curve.

Flow cytometry and analysis
Femurs were dissected out and crushed with a mortar and pestle in ice-cold PBS. Bone marrow solution was passed through a 100-μm filter and pelleted. RBC lysis (ChemCruz) followed as explained above. Cells were resuspended in PBS and stained for total ECs: primary antibody CD45 (BD Pharmingen, 1:100) or type-H ECs: primary antibody endomucin (Santa Cruz Biotechnology, 1:50) and secondary antibody Brilliant Violet-421 (Jackson ImmunoResearch, 1:50) along with CD31-PE (Miltenyi Biotec, 1:20) or CD31-APC (Miltenyi Biotec, 1:20). Mitochondrial staining was performed after antibody incubations with MitoSOX (Thermo Fisher Scientific, 1 μM) for 15 minutes at 37 °C. Cells were run through the BD LSR II flow cytometer using BD FACSDiva 9.0.0 software.

For FABP4 staining, anti-FABP4-AF488 (Santa Cruz Biotechnology, 1:50) was added along with anti-CD31-PE after primary anti-CD45 incubation.

For Ki-67 staining, cells were stained as explained above for total endothelium. After secondary antibody staining and washes, cells were fixed, permeabilized (0.1% BSA and 0.01% saponin) and stained with FITC anti-mouse Ki-67 (BioLegend, 1:75) for 45 minutes at room temperature, and cells were acquired on a BD LSR II flow cytometer.

To detect intracellular ferrous ions, cells were incubated with FeRhoNox-1 (Goryo Chemical, 5 μM) for 15 minutes at 37 °C after staining for total ECs.

BECs in culture, treated with vehicle (DMSO) or 17β-estradiol (10 μM) were trypsinized, pelleted and incubated with either BODIPY 558/568 C12 (Thermo Fisher Scientific, 1 μM) or HCS LipidTOX Green (Thermo Fisher Scientific, 1:1,000) for 30 minutes at 37 °C before acquisition.

For the LPO sensor, cells were stained for total endothelium and then incubated with BODIPY 665/676 (Thermo Fisher Scientific, 2 μg ml^{-1}) for 30 minutes at 37 °C before acquisition.

All flow cytometry analysis was done using FlowJo 10.0.0 software. Total ECs were gated for CD31$^+$CD45$^-$Ter119$^-$ populations, and type-H ECs were gated for Emcn^{high}/CD31^{high} populations.

Metabolic assays
Radioactive assays. BECs were seeded at approximately 25,000 cells per well for all radioisotope labeling experiments and were treated with vehicle (DMSO) or 17β-estradiol for 48 hours before radiolabeling. To measure glucose and glutamine oxidation, cells were incubated with 0.3 μCi/ml D-[6-^{14}C]-glucose (PerkinElmer) or 1.1 μCi/ml L-[^{14}C(U)]-glutamine (PerkinElmer) in cell culture medium for 6 hours. To stop cellular metabolism, 250 μl of perchloric acid was added to each well with the addition of a filter paper soaked in hyamine hydroxide to absorb ^{14}CO$_2$ released by glucose or glutamine oxidation overnight at room temperature. Radioactivity was determined by liquid scintillation counting to denote disintegrations per minute. For the FA oxidation study, etomoxir was used to inhibit CPT1A as described before. To measure palmitate oxidation, cells were incubated with 2 μCi/ml [9,10-^{3}H]-palmitic acid (PerkinElmer) in the cell culture medium for 6 hours. The cell culture medium was transferred to glass vials with hanging filter paper to absorb ^{3}H$_2$O released over 48 hours at 37 °C. Radioactivity was determined by liquid scintillation counting (QuantaSmart) to denote disintegrations per minute.

Image processing and quantification
Z-stacks of images were reconstructed in 3D and analyzed using Imaris Image Analysis software version 9.0.0. Perilipin$^+$ and type-H area

quantification was done using ImageJ (Fiji) on the maximum projection of Z-stacks. Osterix⁺ cell numbers were automatically counted using the spots detection feature by setting a threshold diameter for osterix⁺ nuclei to exclude background using Imaris. Type-H vessel volume was quantified using the surfaces feature to generate 3D overlaps of Emcn⁺CD31⁺ volumes in Imaris. EdU⁺ ECs were automatically counted using the spots feature detection in Imaris, similarly to osterix⁺ nuclei, after applying a mask for Emcn⁺ blood vessels using the surfaces feature. Ki-67⁺ ECs were quantified similarly. Mean fluorescence intensity (MFI) for Emcn⁺ 4-HNE and FABP4 was automatically generated during the 3D reconstruction of Z-stacks for volume analysis by creating a mask for Emcn⁺ vessels. CD31⁺Ki-67⁺ cell nuclei were counted using the cell counter function in ImageJ (Fiji). CD31⁺ 4-HNE (MFI) for cells were generated in ImageJ (Fiji) by using the integrated density and mean gray values. Background fluorescence was subtracted to obtain corrected fluorescence intensity per cell across several images. Plin⁺ ATGL and HSL (MFI) were calculated in a similar way, using integrated density and mean gray values per lipid droplet across several images for 4–5 bone samples.

qRT–PCR
ECs were isolated with antibody-coated beads, as explained above. Instead of plating cells for culture, cells were lysed with RLT buffer (Qiagen), and RNA was extracted using the RNeasy Plus Micro Kit (Qiagen, 74034) as per the manufacturer's guidelines. Total RNA was converted to cDNA using the iScript cDNA Synthesis Kit (Bio-Rad) according to kit instructions. Diluted cDNA was used for qPCR performed using SYBR Green Master Mix (Thermo Fisher Scientific) with primers for the following genes: *Tgfb*, *Eng*, *Tie1*, *Pecam1*, *Itga5*, *Flt4*, *Flt1*, *Fgfr2*, *Sox18*, *Nrp1*, *Adipoq*, *Fabp4*, *Cyp1b1*, *Lepr*, *Aldh1a2*, *TNFα* and *Il6*. β-*actin* was used as a housekeeping gene.

To confirm the loss of gene function at the transcript level for gene deletion experiments, ECs were isolated from femurs of tamoxifen-injected transgenic mice for qPCR using primers for each gene (*Esr1*, *Esr2*, *Gper1* and *Cpt1a*). Primer sequences used in this study are provided in Supplementary Table 1.

Reactions were run on a CFX real-time PCR machine (Bio-Rad) using CFX manager 3.1 software. Data were calculated using the ΔΔCt method to show fold gene expression or relative mRNA levels.

RNA-seq
Isolated bone ECs were lysed using RLT buffer. RNA was extracted using the RNeasy Plus Micro Kit as per the manufacturer's guidelines.

Library preparation. The quality of RNA for each individual sample was checked using a 2100 Bioanalyzer (Agilent). The top three samples from each set based on RNA quality were processed further for library preparations. TruSeq Total RNA Library Preparation Kit (Illumina) was used to prepare libraries, following the manufacturer's guidelines. Libraries were sequenced at the LMS Genomics Facility on an Illumina HiSeq 2500 platform with 100-nucleotide-length paired-end reads.

Data analysis: Paired-end 100-bp RNA-seq reads were aligned using the mouse genome assembly GRCm39 STAR (version 2.7.10a)[45]. Gene-based read count was obtained using featureCounts (version 2.0.1)[46]. The count data were normalized using the variance stabilizing transformation (VST) function from the DESeq2 package[47] for visualization by PCA. Differential gene expression analysis between the males versus females for each age group was performed using DESeq2. DE genes were selected (protein coding) using a false discovery rate (FDR)-adjusted *P* < 0.05. Furthermore, the Ensembl IDs were annotated to gene symbols and Entrez Gene ID using biomaRt (ref. [48]). The differentially regulated genes list is provided in Supplementary Dataset 1. Gene set enrichment analysis was performed using GAGE (version 2.42.0)[19]. For functional annotation, we used gene sets from the KEGG database. The GAGE analysis was performed on differentially

regulated genes from 65 weeks of data, where the female sample was taken as a reference sample. The significant KEGG terms were selected using *P* < 0.05.

Statistical methods
GraphPad Prism version 9.4.1 was used for generating all graphs and for statistical analysis. Statistics performed for each figure are mentioned in the corresponding figure legend. Where indicated, Student's two-tailed unpaired *t*-tests or one-way or two-way ANOVA after Tukey's multiple comparison test were performed for datasets. Error bars for biological data indicate mean ± s.d., and, for numerical quantification, error bars indicate mean ± s.e.m. *P* < 0.05 was considered statistically significant. Sample sizes were selected based on previous experiments and published data. All data were generated using at least two independent experiments to reproduce similar results.

Reporting summary
Further information on research design is available in the Nature Research Reporting Summary linked to this article.

Data availability
RNA-seq data generated for this study have been deposited in the National Center for Biotechnology Information Gene Expression Omnibus database under accession numbers GSE163515 and GSE180246. Additional data supporting the findings in this study are included in the main article and associated files. Source data are provided with this paper.

References
1. Clarke, B. L. & Khosla, S. Female reproductive system and bone. *Arch. Biochem. Biophys.* **503**, 118–128 (2010).
2. Khosla, S. & Monroe, D. G. Regulation of bone metabolism by sex steroids. *Cold Spring Harb. Perspect. Med.* **8**, a031211 (2018).
3. Nakada, D. et al. Oestrogen increases haematopoietic stem-cell self-renewal in females and during pregnancy. *Nature* **505**, 555–558 (2014).
4. Zhou, S. et al. Estrogens activate bone morphogenetic protein-2 gene transcription in mouse mesenchymal stem cells. *Mol. Endocrinol.* **17**, 56–66 (2003).
5. Sivan, U., De Angelis, J. & Kusumbe, A. P. Role of angiocrine signals in bone development, homeostasis and disease. *Open Biol.* **9**, 190144 (2019).
6. Hendriks, M. & Ramasamy, S. K. Blood vessels and vascular niches in bone development and physiological remodeling. *Front. Cell Dev. Biol.* **8**, 602278 (2020).
7. Chen, J., Hendriks, M., Chatzis, A., Ramasamy, S. K. & Kusumbe, A. P. Bone vasculature and bone marrow vascular niches in health and disease. *J. Bone Miner. Res.* **35**, 2103–2120 (2020).
8. Kusumbe, A. P., Ramasamy, S. K., Starsichova, A. & Adams, R. H. Sample preparation for high-resolution 3D confocal imaging of mouse skeletal tissue. *Nat. Protoc.* **10**, 1904–1914 (2015).
9. Kusumbe, A. P., Ramasamy, S. K. & Adams, R. H. Coupling of angiogenesis and osteogenesis by a specific vessel subtype in bone. *Nature* **507**, 323–328 (2014).
10. Ramasamy, S. K., Kusumbe, A. P., Wang, L. & Adams, R. H. Endothelial Notch activity promotes angiogenesis and osteogenesis in bone. *Nature* **507**, 376–380 (2014).
11. Borman, S. M., Christian, P. J., Sipes, I. G. & Hoyer, P. B. Ovotoxicity in female Fischer rats and B6 mice induced by low-dose exposure to three polycyclic aromatic hydrocarbons: comparison through calculation of an ovotoxic index. *Toxicol. Appl. Pharmacol.* **167**, 191–198 (2000).
12. Brooks, H. L., Pollow, D. P. & Hoyer, P. B. The VCD mouse model of menopause and perimenopause for the study of sex differences in cardiovascular disease and the metabolic syndrome. *Physiology (Bethesda)* **31**, 250–257 (2016).

13. Kalu, D. N. The ovariectomised rat model of postmenopausal bone loss. *Bone Miner*. **15**, 175–191 (1991).

14. Feng, Y., Manka, D., Wagner, K. U. & Khan, S. A. Estrogen receptor-α expression in the mammary epithelium is required for ductal and alveolar morphogenesis in mice. *Proc. Natl Acad. Sci. USA* **104**, 14718–14723 (2007).

15. Maneix, L. et al. Estrogen receptor β exon 3-deleted mouse: the importance of non-ERE pathways in ERβ signaling. *Proc. Natl Acad. Sci. USA* **112**, 5135–5140 (2015).

16. Wang, H. et al. Cardiomyocyte-specific deletion of the G protein-coupled estrogen receptor (GPER) leads to left ventricular dysfunction and adverse remodeling: a sex-specific gene profiling analysis. *Biochim. Biophys. Acta Mol. Basis Dis.* **1863**, 1870–1882 (2017).

17. Wang, Y. et al. Ephrin-B2 controls VEGF-induced angiogenesis and lymphangiogenesis. *Nature* **465**, 483–486 (2010).

18. Romeo, S. G. et al. Endothelial proteolytic activity and interaction with non-resorbing osteoclasts mediate bone elongation. *Nat. Cell Biol.* **21**, 430–441 (2019).

19. Luo, W., Friedman, M. S., Shedden, K., Hankenson, K. D. & Woolf, P. J. GAGE: generally applicable gene set enrichment for pathway analysis. *BMC Bioinformatics* **10**, 161 (2009).

20. De Bock, K. et al. Role of PFKFB3-driven glycolysis in vessel sprouting. *Cell* **154**, 651–663 (2013).

21. Schoors, S. et al. Fatty acid carbon is essential for dNTP synthesis in endothelial cells. *Nature* **520**, 192–197 (2015).

22. Huang, H. et al. Role of glutamine and interlinked asparagine metabolism in vessel formation. *EMBO J.* **36**, 2334–2352 (2017).

23. Shafat, M. S. et al. Leukemic blasts program bone marrow adipocytes to generate a protumoral microenvironment. *Blood* **129**, 1320–1332 (2017).

24. Kusumbe, A. P. et al. Age-dependent modulation of vascular niches for haematopoietic stem cells. *Nature* **532**, 380–384 (2016).

25. Ramasamy, S. K. et al. Blood flow controls bone vascular function and osteogenesis. *Nat. Commun.* **7**, 13601 (2016).

26. Devlin, M. J. & Rosen, C. J. The bone–fat interface: basic and clinical implications of marrow adiposity. *Lancet Diabetes Endocrinol.* **3**, 141–147 (2015).

27. Kawai, M., de Paula, F. J. & Rosen, C. J. New insights into osteoporosis: the bone–fat connection. *J. Intern. Med.* **272**, 317–329 (2012).

28. Cooke, P. S. & Naaz, A. Role of estrogens in adipocyte development and function. *Exp. Biol. Med. (Maywood)* **229**, 1127–1135 (2004).

29. Okazaki, R. et al. Estrogen promotes early osteoblast differentiation and inhibits adipocyte differentiation in mouse bone marrow stromal cell lines that express estrogen receptor (ER) α or β. *Endocrinology* **143**, 2349–2356 (2002).

30. Goodman-Gruen, D. & Barrett-Connor, E. Sex differences in the association of endogenous sex hormone levels and glucose tolerance status in older men and women. *Diabetes Care* **23**, 912–918 (2000).

31. Carani, C. et al. Effect of testosterone and estradiol in a man with aromatase deficiency. *N. Engl. J. Med.* **337**, 91–95 (1997).

32. Ferrini, R. L. & Barrett-Connor, E. Sex hormones and age: a cross-sectional study of testosterone and estradiol and their bioavailable fractions in community-dwelling men. *Am. J. Epidemiol.* **147**, 750–754 (1998).

33. Lindle, R. S. et al. Age and gender comparisons of muscle strength in 654 women and men aged 20–93 yr. *J. Appl. Physiol. (1985)* **83**, 1581–1587 (1997).

34. Hofbauer, L. C. et al. Estrogen stimulates gene expression and protein production of osteoprotegerin in human osteoblastic cells. *Endocrinology* **140**, 4367–4370 (1999).

35. Bord, S., Ireland, D. C., Beavan, S. R. & Compston, J. E. The effects of estrogen on osteoprotegerin, RANKL, and estrogen receptor expression in human osteoblasts. *Bone* **32**, 136–141 (2003).

36. Saika, M., Inoue, D., Kido, S. & Matsumoto, T. 17β-estradiol stimulates expression of osteoprotegerin by a mouse stromal cell line, ST-2, via estrogen receptor-α. *Endocrinology* **142**, 2205–2212 (2001).

37. Streicher, C. et al. Estrogen regulates bone turnover by targeting RANKL expression in bone lining cells. *Sci. Rep.* **7**, 6460 (2017).

38. Kourtis, N. & Tavernarakis, N. Cellular stress response pathways and ageing: intricate molecular relationships. *EMBO J.* **30**, 2520–2531 (2011).

39. Schaur, R. J. Basic aspects of the biochemical reactivity of 4-hydroxynonenal. *Mol. Aspects Med.* **24**, 149–159 (2003).

40. Kajimoto, K., Minami, Y. & Harashima, H. Cytoprotective role of the fatty acid binding protein 4 against oxidative and endoplasmic reticulum stress in 3T3-L1 adipocytes. *FEBS Open Bio.* **4**, 602–610 (2014).

41. Dixon, S. J. et al. Ferroptosis: an iron-dependent form of nonapoptotic cell death. *Cell* **149**, 1060–1072 (2012).

42. Friedmann Angeli, J. P. et al. Inactivation of the ferroptosis regulator Gpx4 triggers acute renal failure in mice. *Nat. Cell Biol.* **16**, 1180–1191 (2014).

43. Syed, F. A. et al. Effects of estrogen therapy on bone marrow adipocytes in postmenopausal osteoporotic women. *Osteoporos. Int.* **19**, 1323–1330 (2008).

44. Chen, J. et al. High-resolution 3D imaging uncovers organ-specific vascular control of tissue aging. *Sci. Adv.* **7**, eabd7819 (2021).

45. Dobin, A. et al. STAR: ultrafast universal RNA-seq aligner. *Bioinformatics* **29**, 15–21 (2013).

46. Liao, Y., Smyth, G. K. & Shi, W. featureCounts: an efficient general purpose program for assigning sequence reads to genomic features. *Bioinformatics* **30**, 923–930 (2014).

47. Love, M. I., Huber, W. & Anders, S. Moderated estimation of fold change and dispersion for RNA-seq data with DESeq2. *Genome Biol.* **15**, 550 (2014).

48. Durinck, S., Spellman, P. T., Birney, E. & Huber, W. Mapping identifiers for the integration of genomic datasets with the R/ Bioconductor package biomaRt. *Nat. Protoc.* **4**, 1184–1191 (2009).

Acknowledgements

Author contributions

J.R. designed and performed most of the experiments, interpreted results and prepared figures. Y.-F.W., A.S. and G.D. analyzed gene expression data. M.H. sorted cells and prepared the manuscript. A.P.K. designed experiments and interpreted results. All authors prepared the manuscript. S.K.R. conceived and supervised the study, interpreted the results and wrote the manuscript.

Competing interests

The authors declare no competing financial interests.

Additional information

Extended data is available for this paper at https://doi.org/10.1038/s44161-022-00139-0.

Supplementary information The online version contains supplementary material available at https://doi.org/10.1038/s44161-022-00139-0.

Correspondence and requests for materials should be addressed to Saravana K. Ramasamy.

Peer review information *Nature Cardiovascular Research* thanks Philip Shaul, Joshua Farr and the other, anonymous, reviewer(s) for their contribution to the peer review of this work.

Reprints and permissions information is available at www.nature.com/reprints.

Publisher's note Springer Nature remains neutral with regard to jurisdictional claims in published maps and institutional affiliations.

Extended Data Fig. 1 | See next page for caption.

Extended Data Fig. 1 | Changes in the frequency of OBLs and adipocytes during pregnancy and menopause. a, Representative confocal images showing changes in OBLs (Osterix+) and bone marrow (BM) adipocytes (Perilipin+) at different time-points during mouse pregnancy and *post-partum*. Scale bars 40 μm. **b**, Quantification of OBLs and BM adipocytes described in **a**, normalised to metaphysis (mp) length and area respectively (n = 5). Data are mean ± s.d.; One-Way ANOVA with Tukey's test. **c**, Quantification of Ki-67+ ECs at different time-points during mouse pregnancy, normalised to the length of mp (n = 5). Data are mean ± s.d.; One-Way ANOVA with Tukey's test. **d**, Representative confocal images with quantifications (n = 5) showing loss of OBLs, and increase in BM adipocytes in the VCD model. Data are mean ± s.d.; Unpaired two-tailed t-test. Scale bars 40 μm. **e**, Representative confocal tile scans of Vehicle and E2-treated bones at P28, illustrating increased Type-H vessels (arrowheads) in E2-treated mice. White dotted lines separate bone marrow from the cortical bone region. Quantification of Type-H ECs (CD31^{high} Emcn^{high}) characterised by flow cytometry (n = 6). Data are mean ± s.e.m.; Two-way ANOVA with Tukey's test. Scale bars 100 μm.
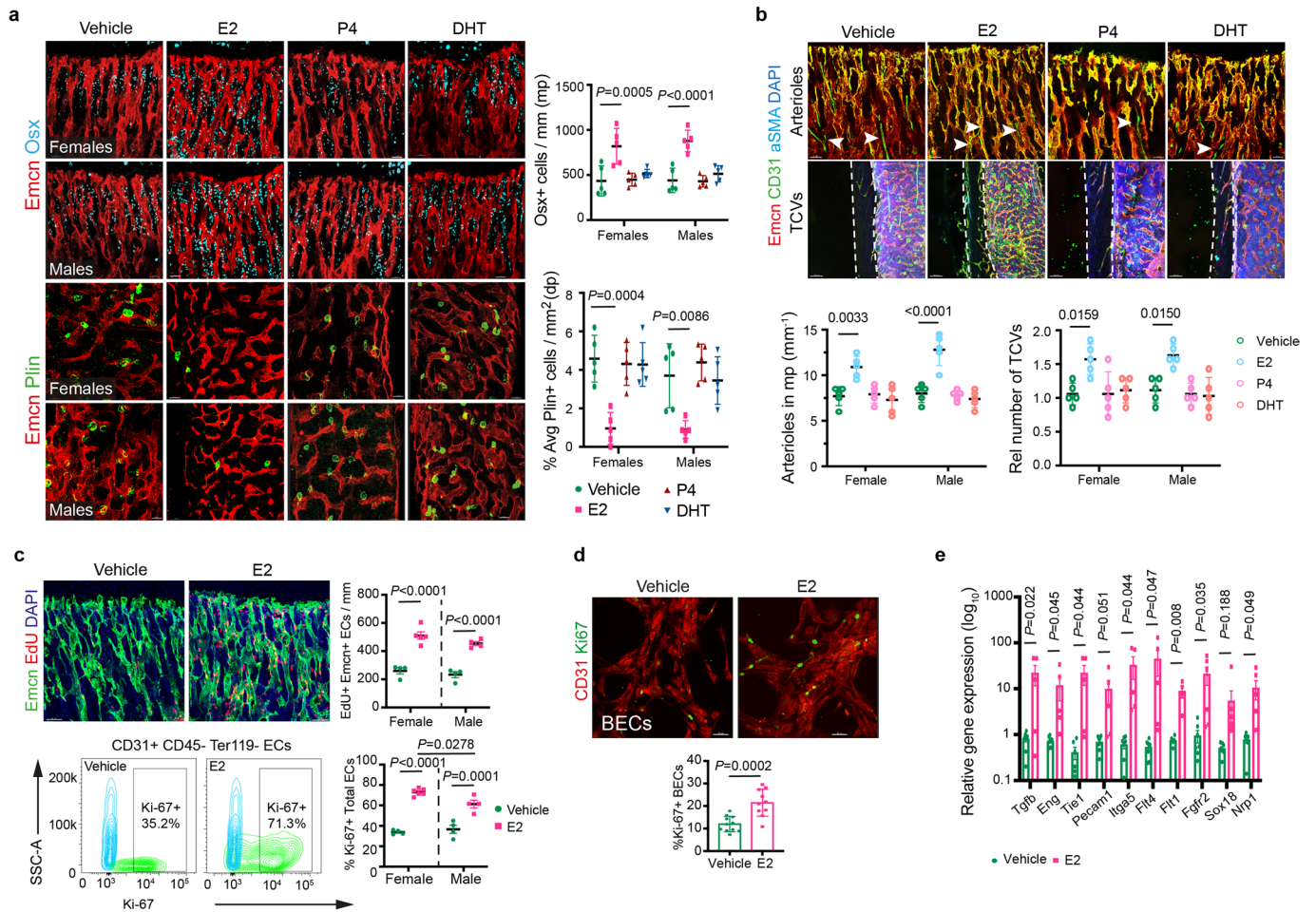
Extended Data Fig. 2 | Oestrogen-mediated changes in bone endothelium.
a, Representative confocal images with quantifications of OBLs (Osterix+, n = 5) and BM adipocytes (Perilipin + , n = 5) of mice treated with different hormones at P28. Data are mean ± s.d.; Two-way ANOVA with Tukey's test. Scale bars 40 μm. **b**, Representative confocal images show endomucin (Emcn, red), CD31 (green), alpha-smooth muscle actin (αSMA, cyan) blood vessels in the metaphysis and cortical bone area. Graphs show quantification of CD31 + Emcn- arterioles (white arrowheads) and TCVs in mice treated with Vehicle, E2, P4 and DHT (n = 5); Data are mean ± s.d.; Two-way ANOVA with Tukey's test. White dotted lines denote the cortical bone region. DAPI is a nuclear counterstain. Scale bars 100 μm (TCVs); 50 μm (arterioles). **c**, Representative confocal images of EdU-injected Vehicle and E2-treated mice at P28, with quantification of EdU+ ECs normalised to metaphysis (mp) length (Vehicle n = 4 F, n = 4 M; E2 n = 5 F, n = 4 M) indicating increased EdU+ ECs with E2 treatment. Scale bars 50 μm. Representative flow cytometry plots of Ki-67+ ECs, with quantification of Ki-67+ ECs in bone (Vehicle

n = 4 F, n = 4 M; E2 n = 6 F, n = 4 M) indicating an increase in Ki-67+ ECs with E2 treatment. Image quantification data are mean ± s.d. with Two-way ANOVA with Tukey's test, and flow cytometry data mean ± s.e.m. with Two-way ANOVA with Tukey's test. **d**, Representative confocal images and quantification of Ki-67+ nuclei of Vehicle and E2-treated BECs (Vehicle n = 11, E2 n = 10) with quantification of average from multiple 20x fields of view indicating an increase in Ki-67+ cells with E2 treatment. Data are mean ± s.d.; Unpaired two-tailed t-test. Scale bars 50 μm. **e**, Graph showing relative gene expression for angiogenic genes in Vehicle and E2-treated mice, indicating an increase in angiogenesis upon E2 treatment. (*Tgfb* Vehicle n = 8, E2 n = 5; *Eng* Vehicle n = 8, E2 n = 5; *Tie1* Vehicle n = 6, E2 n = 5; *Pecam1* Vehicle n = 8, E2 n = 5; *Itga5* Vehicle n = 7, E2 n = 5; *Flt4* Vehicle n = 8, E2 n = 5; *Flt1* Vehicle n = 5, E2 n = 4; *Fgfr2* Vehicle n = 7, E2 n = 6; *Sox18* Vehicle n = 8, E2 n = 8; *Nrp1* Vehicle n = 7, E2 n = 6.) Data are mean ± s.e.m.; Multiple Unpaired two-tailed t-test.
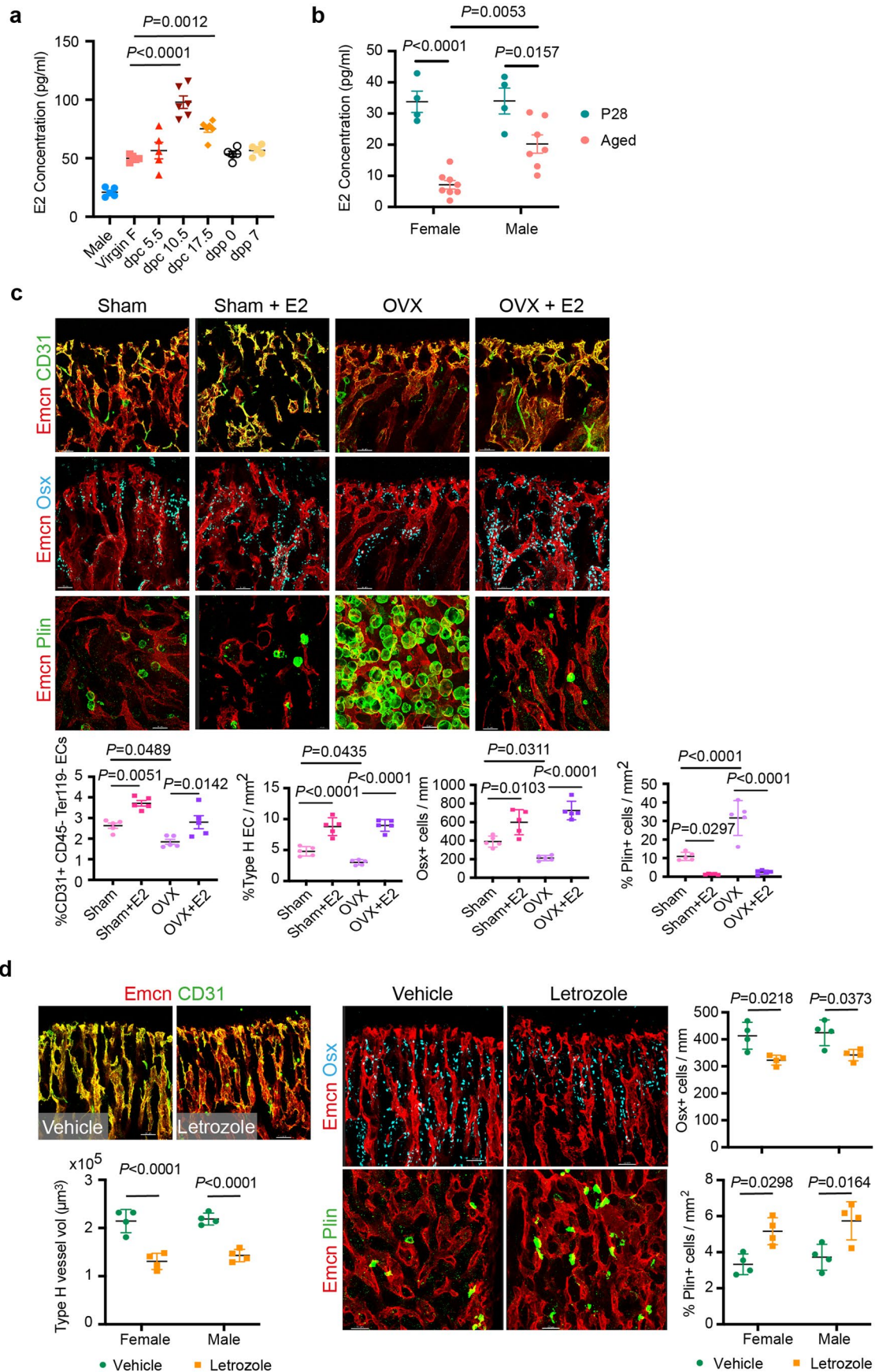
**Extended Data Fig. 3 | See next page for caption.**

Extended Data Fig. 3 | Oestrogen-mediated changes in bone endothelium. a, Graph showing serum E2 concentration at different time-points during mouse pregnancy (n = 6 for dpc10.5, dpc17.5; n = 5 for Male, Virgin F, dpc5.5, dpp0, dpp7). Data are mean ± s.e.m.; One-Way ANOVA with Tukey's test. **b**, Graph showing serum E2 concentration in P28 (n = 4 F, n = 4 M) and aged (n = 8 F, n = 7 M) mice. Data are mean ± s.e.m.; Two-Way ANOVA with Tukey's test. **c**, Representative confocal images with quantifications of Type-H (yellow, Emcn^{high} CD31^{high}) blood vessels (n = 5 for all conditions), OBLs (Osterix + , n = 5), and BM adipocytes (Perilipin + , n = 5) in Vehicle and E2-treated sham-operated and OVX mice. Flow cytometry quantification of total ECs (CD31 + CD45-Ter119-) shows the recovery of BECs in E2-treated bones (n = 5). Data are mean ± s.d. for image quantification and mean ± s.e.m. for flow cytometry data. Two-Way ANOVA with Tukey's test. Scale bars 50 μm. **d**, Bone tissue sections of Vehicle and Letrozole-treated mice at P28 were immunostained with CD31 (green) and Emcn (red) to identify type-H vessels. The graph shows quantifications of Type-H (yellow) blood vessels (n = 4). The distribution of OBLs and BM adipocytes in these bone sections were imaged using Osterix + (cyan) and Perilipin (green). Graphs show quantification of OBLs (n = 4) and adipocytes (n = 4) in Vehicle and Letrozole-treated mice. Data are mean ± s.d.; Two-Way ANOVA with Tukey's test. Scale bars 50 μm.
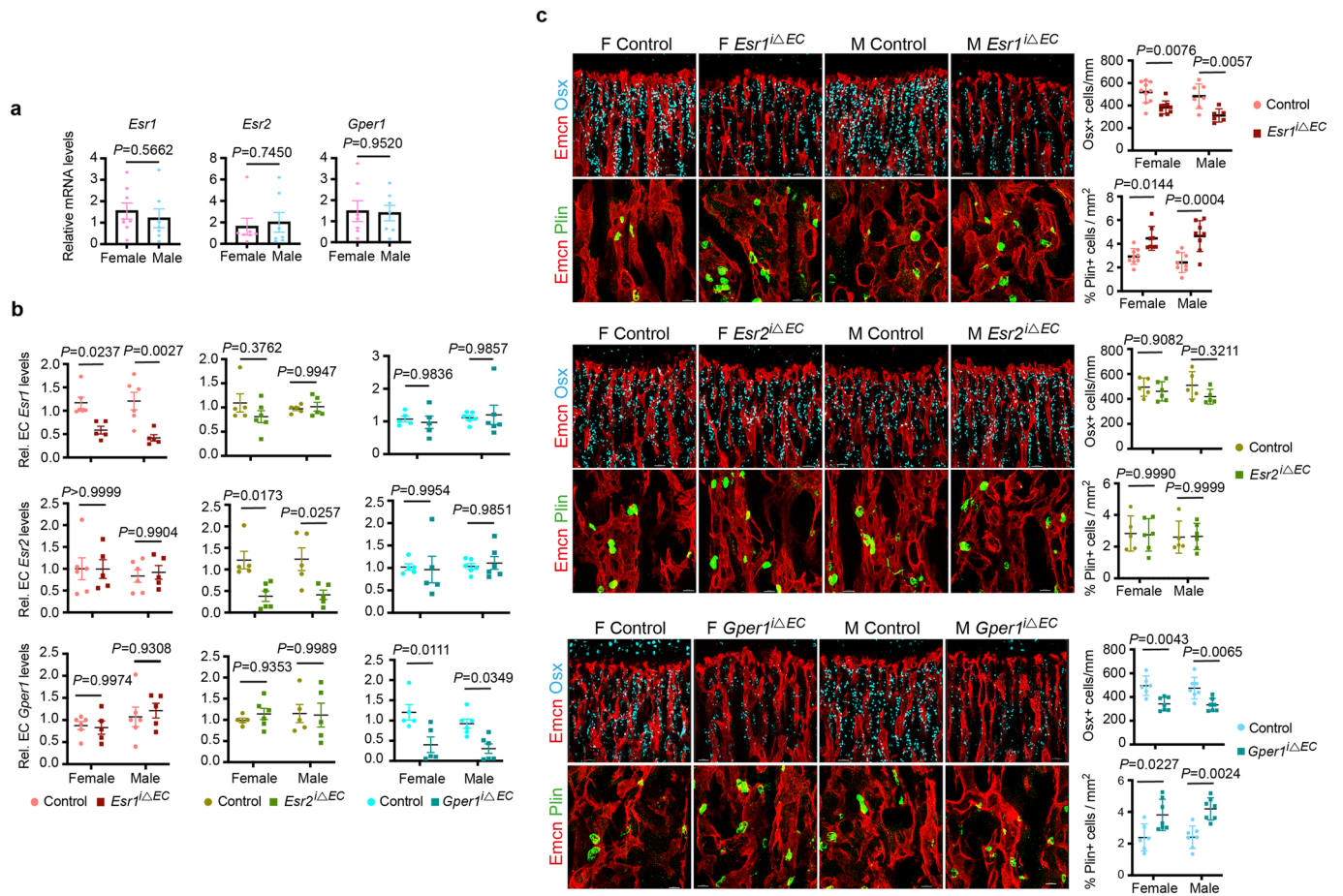
**Extended Data Fig. 4 | Cellular changes in the bone microenvironment of endothelial-specific oestrogen receptor deletion mutants. a**, Graphs indicating relative mRNA levels of oestrogen receptors *(Esr1, Esr2, Gper1)* in female and male BECs at P28. *(Esr1*: n = 8 F, n = 7 M; *Esr2, Gper1*: n = 7) Data are mean ± s.e.m.; Unpaired two-tailed t-test. **b**, Graphs showing ER transcript levels in purified BECs of endothelial *Esr1, Esr2,* or *Gper1* deletion mutant and control littermates (*Esr1* Control n = 6 F, n = 6 M, Mutant n = 5 F, n = 5 M; *Esr2* Control n = 5 F, n = 5 M, Mutant n = 6 F, n = 5 M; *Gper1* Control n = 5 F, n = 6 M, Mutant n = 5 F, n = 6 M). Data are mean ± s.e.m.; Two-Way ANOVA with Tukey's test. **c**,

Representative confocal images of mutants with endothelial *Esr1, Esr2,* or *Gper1* deletion compared to littermate Cre- controls, with quantifications showing loss of OBLs, and increase in adipocytes after *Esr1* and *Gper1* deletion (*Esr1*:Osx-Control n = 10 F, n = 7 M, Mutant n = 9 F, n = 6 M; *Esr1*:Plin-Control n = 9 F, n = 8 M, Mutant n = 8 F, n = 8 M; *Esr2*:Osx-Control n = 5 F, n = 5 M, Mutant n = 6 F, n = 5 M; *Esr2*:Plin Control n = 5 F, n = 5 M, Mutant n = 6 F, n = 6 M; *Gper1*: both Osx and Plin-Control n = 6 F, n = 7 M, Mutant n = 7 F, n = 7 M). Data are mean ± s.d.; Two-Way ANOVA with Tukey's test. Scale bars 40 μm.
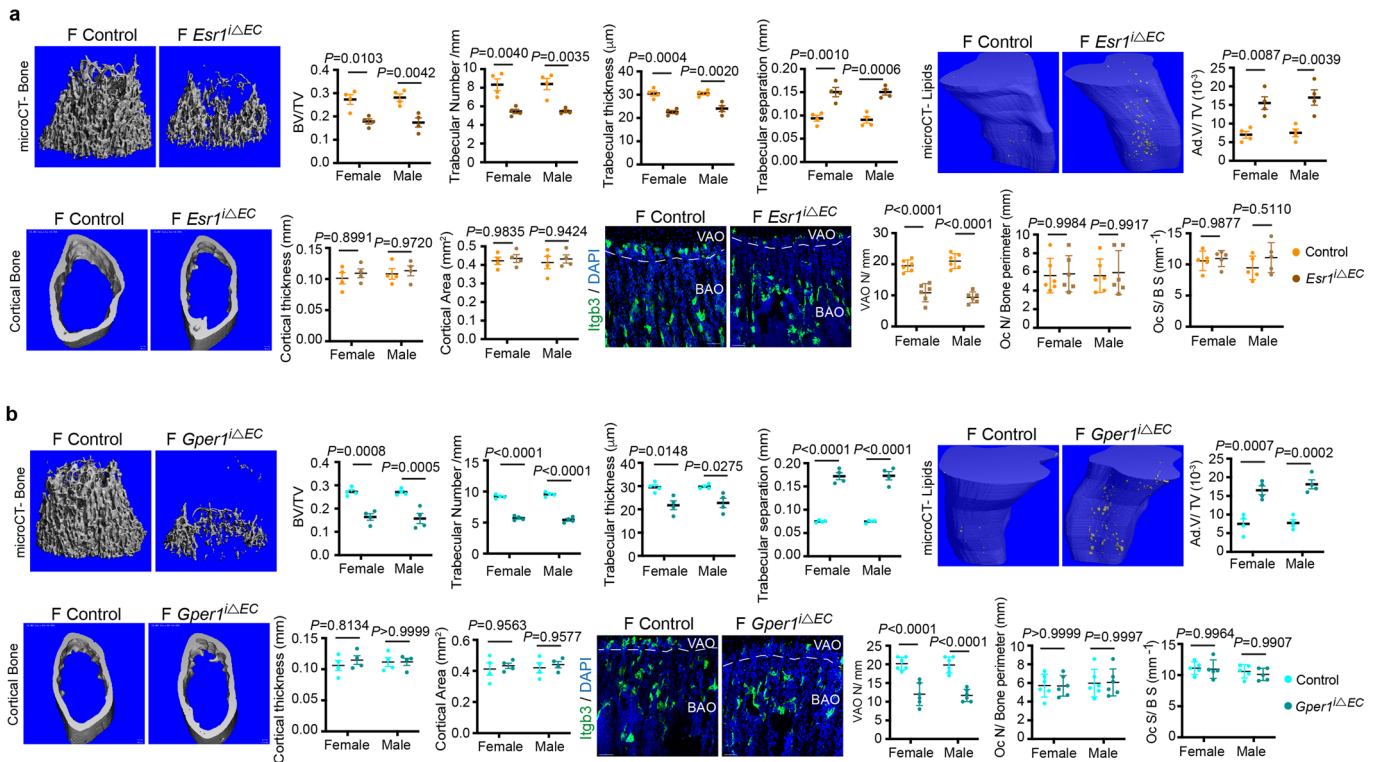
Extended Data Fig. 5 | Phenotype analysis of endothelial ER mutants. a, Representative microCT analysis of mutants with endothelial *Esr1* deletion compared to littermate Cre- controls, with quantifications showing trabecular bone volume fraction (BV/TV), number, thickness and separation (n = 4), quantification of adipocytes (n = 4) and cortical bone quantification of thickness and area (n = 4). Representative confocal images show osteoclasts distribution in control and mutant bones with quantification of osteoclasts number (n = 6) and coverage (n = 5). Data are mean ± s.e.m. for micro-CT results and ± s.d for image quantification; Two-Way ANOVA with Tukey's test. Scale bars 100 µm

(microCT), 50 µm (confocal). **b**, Representative microCT images of mutants with endothelial *Gper1* deletion compared to littermate Cre- controls, with quantifications showing trabecular bone volume fraction (BV/TV), number, thickness, and separation (n = 4), quantification of adipocytes (n = 4) and cortical bone quantification of thickness and area (n = 4). Representative confocal images show osteoclasts distribution in control and mutant bones with quantification of osteoclasts number (n = 6) and coverage (n = 5). Data are mean ± s.e.m. for micro-CT results and ± s.d for image quantification; Two-Way ANOVA with Tukey's test. Scale bars 100 µm (microCT), 50 µm (confocal).
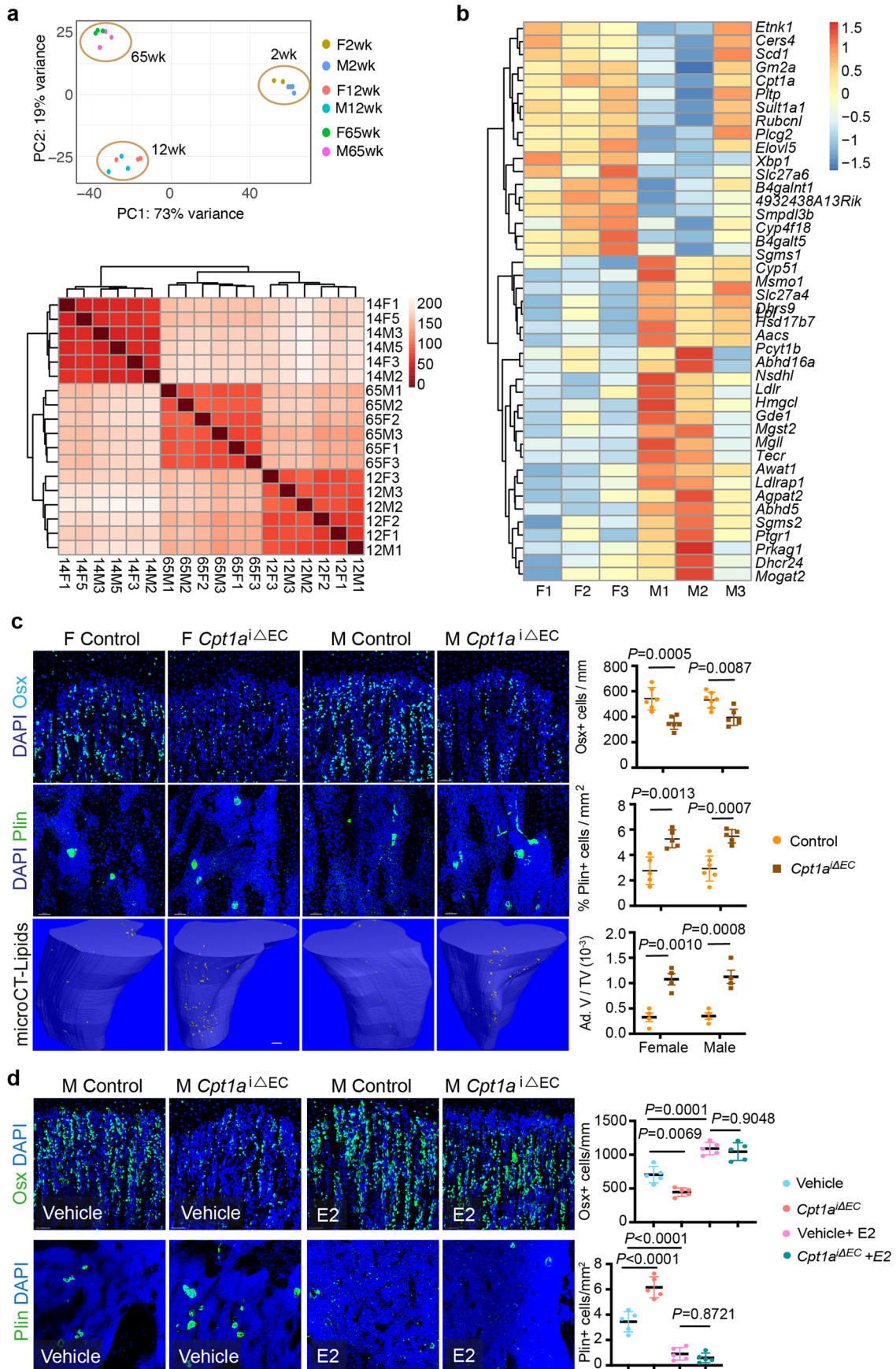
Extended Data Fig. 6 | See next page for caption.

Extended Data Fig. 6 | Lipid metabolism of BECs. a, PCA plot of RNAseq data showing clustering of purified male and female BECs from 2 weeks, 12 weeks, and 65 weeks old mice (n = 3). Sample correlation heatmap of gene expression pattern show clustering of age groups. **b**, Heatmap showing genes associated with fatty acid metabolism, which are differentially expressed in aged mouse BECs between males and females. **c**, Representative confocal images showing cell types within the BM microenvironment of *Cpt1a* mutants with graphs showing quantification of Osterix+ cells per mm of mp (Control n = 6 F, n = 7 M; Mutant n = 6 F, n = 6 M); Perilipin+ area per mm^2 area (Control n = 5 F, n = 6 M; Mutant

n = 5 F, n = 5 M). Representative microCT images with quantification show an increase in BM adipocyte volume in *Cpt1a* mutants (n = 4). Data are mean ± s.d for image quantification and mean ± s.e.m for microCT data; Two-Way ANOVA with Tukey's test. Scale bars 100 μm (microCT), 40 μm (confocal). **d**, Representative confocal images show Osx+ cells and Perilipin+ adipocytes in male control and *Cpt1a*^{iΔEC} mutant mice treated with E2. Graphs show quantifications of Osx+ cells per mm of mp (n = 5) and Perilipin+ cells per mm^2 (n = 5). Data are mean ± s.d.; Two-Way ANOVA with Tukey's test. Scale bars 50 μm.
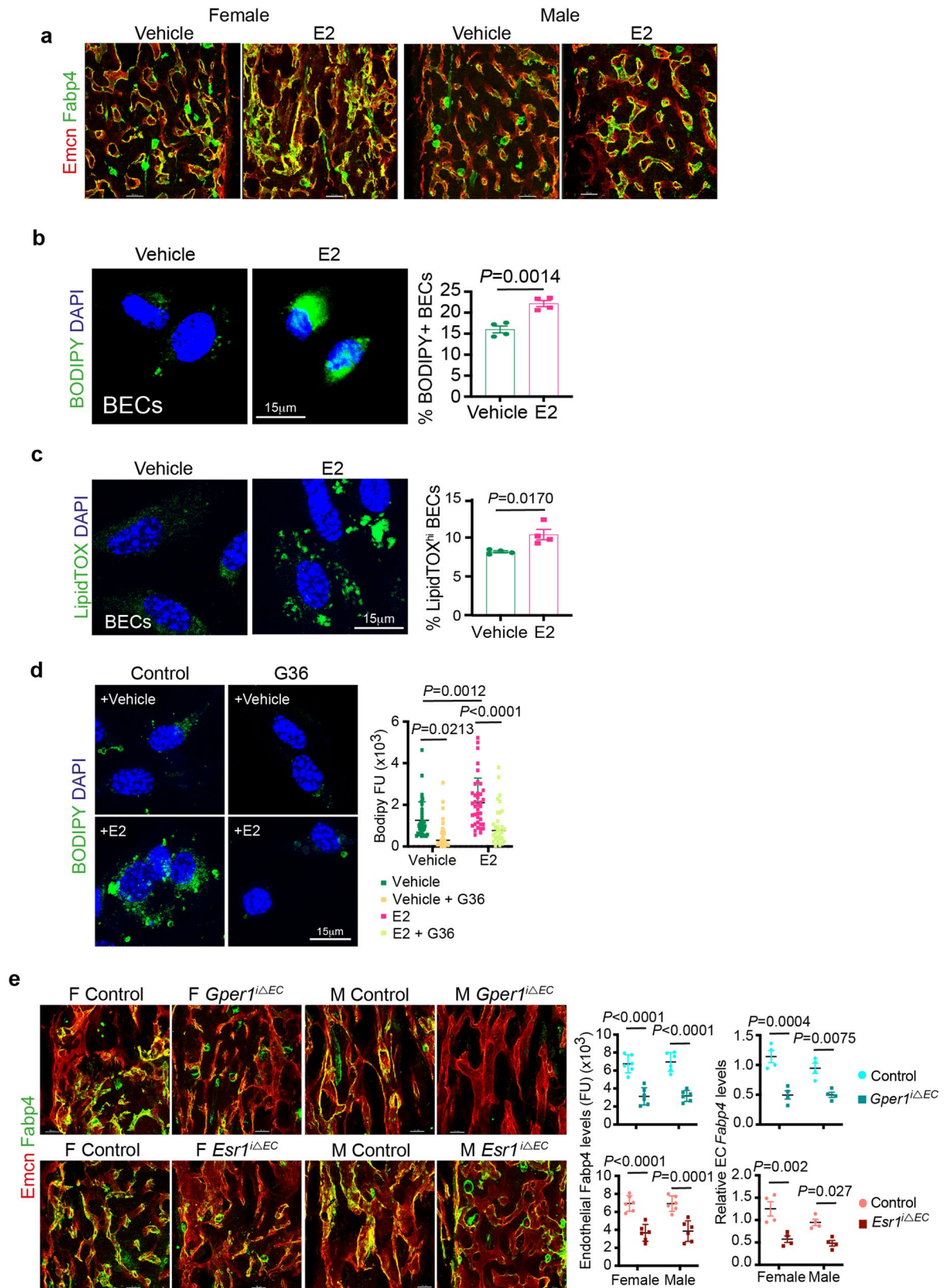
Extended Data Fig. 7 | See next page for caption.

Extended Data Fig. 7 | Lipid transport mechanism in BECs. a, Immunostainings show FABP4 expression (green) in blood vessels (Emcn, red) of vehicle and E2 treated tibia of both male and female mice (n = 7). Scale bars 50 μm. **b**, Representative confocal images of lipid uptake of BODIPY-conjugated synthetic FAs in Vehicle and E2-treated BECs (n = 4), with quantification by flow cytometry indicating an increase in lipid uptake with E2 treatment. Data are mean ± s.e.m.; Unpaired two-tailed t-test. Scale bars 15 μm. **c**, Representative confocal images of intracellular lipid levels in Vehicle and E2-treated BECs. The graph shows flow cytometry quantification of BECs having high LipidTOX (n = 4) levels in vehicle and E2 conditions. Data are mean ± s.e.m.; Unpaired two-tailed t-test. Scale bars 15 μm. **d**, Representative confocal images of lipid uptake of BODIPY-conjugated synthetic FAs in Vehicle and E2-treated BECs upon GPER1 inhibitor

G36 treatment. Quantification shows reduced fluorescence units of endothelial BODIPY upon GPER1 inhibition, across multiple 63x fields of view (Vehicle n = 37, Vehicle+G36 n = 30; E2 n = 39, E2 + G36 n = 30). Data are mean ± s.d.; Two-Way ANOVA with Tukey's test. Scale bars 15 μm. **e**, Representative confocal images and quantification of endothelial FABP4 levels in mice with oestrogen-receptor deletions *Esr1* (Control n = 6 F, n = 6 M; Mutant n = 6 F, n = 6 M) and *Gper1* (Control n = 6 F, n = 6 M; Mutant n = 6 F, n = 6 M). Data are mean ± s.d.; Two-Way ANOVA with Tukey's test. Relative *Fabp4* transcript levels were also quantified in purified endothelial cells from endothelial GPER1 (n = 4) and ESR1 (n = 4) mutants compared to their littermate control. Data are mean ± s.e.m; Two-Way ANOVA with Tukey's test. Scale bars 50 μm.
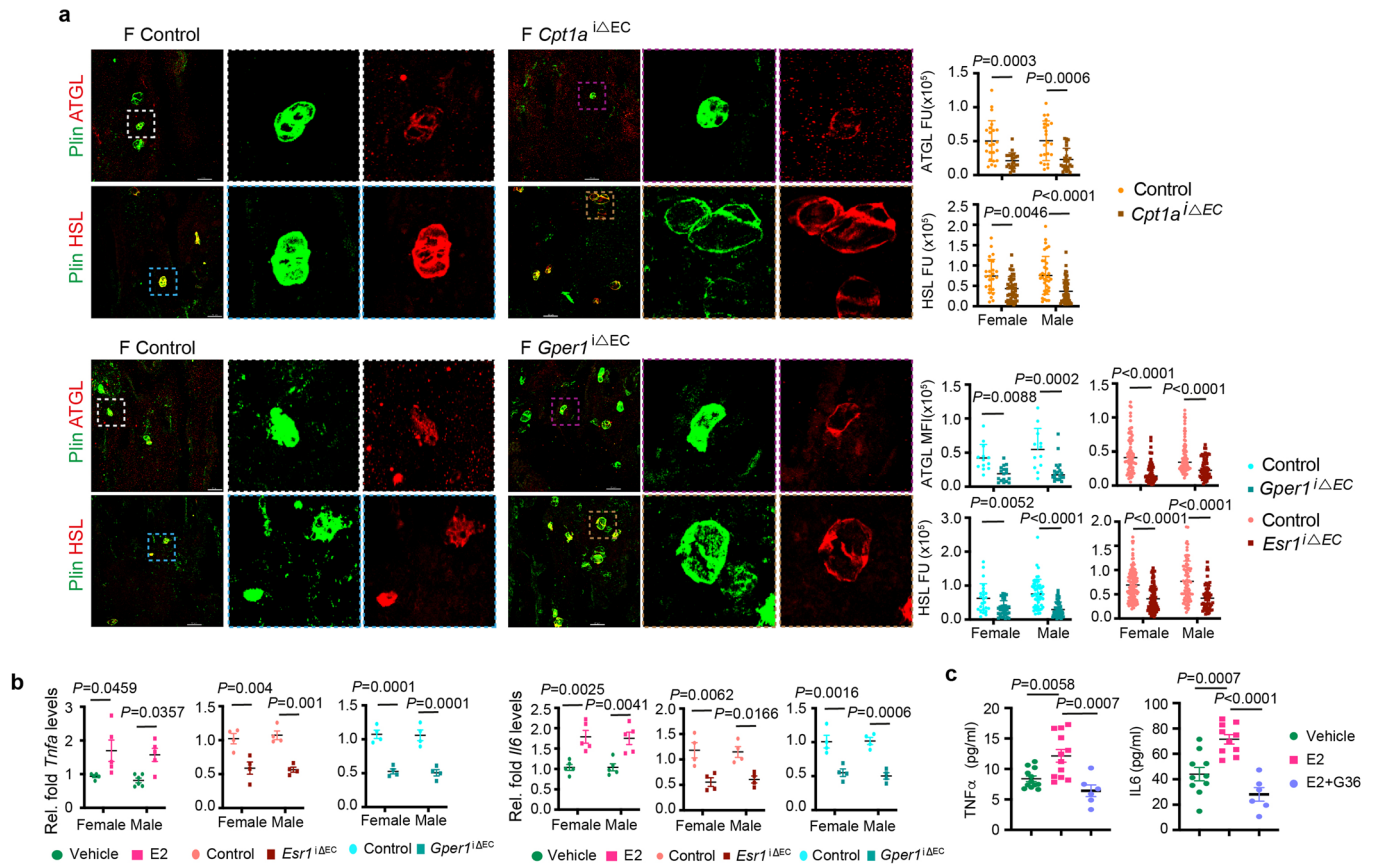
Extended Data Fig. 8 | Metabolic coupling of BECs with adipocytes. a, Representative confocal images of BM adipocytes (Perilipin + cells) and lipolytic enzymes (ATGL and HSL) in *Cpt1a* and *Gper1* mutant bones and their respective littermates. Scale bars 50 μm. Graphs show with fluorescence quantifications indicating a decrease in lipolytic enzymes (ATGL and HSL) in *Cpt1a* (ATGL: Control n = 23 F, 15 M; Mutant n = 23 F, 24 M. HSL Control n = 19 F,36 M; Mutant n = 42 F,54 M), *Gper1* (ATGL: Control n = 13 F,12 M; Mutant n = 17 F, 21 M. HSL: Control n = 19 F,50 M; Mutant n = 37 F,49 M) and *Esr1* (ATGL: Control n = 75 F,72 M; Mutant n = 63 F, 62 M. HSL: Control n = 127 F,79 M; Mutant n = 106 F,60 M)

deletion, per cell across multiple 20x fields of view. Data are mean ± s.d.; Two-Way ANOVA with Tukey's test. **b**, Graphs showing relative transcript levels of *Tnfa* and *Il6* mRNA in isolated BECs of E2-treated mice (Vehicle n = 5 F, n = 5 M; E2 n = 5 F, n = 5 M), and endothelial *Cpt1a* and *Gper1* deletion mutants (control n = 4 F, n = 4 M; mutant n = 4 F, n = 4 M). Data are mean ± s.e.m.; Two-Way ANOVA with Tukey's test. **c**, Graph showing increased TNFα (vehicle n = 12, E2 n = 12, E2 + G36 n = 6) and IL-6 (vehicle n = 12, E2 n = 12, E2 + G36 n = 6) levels quantified from cell culture supernatants of BECs treated with vehicle, E2 and E2 + G36. Data are mean ± s.e.m.; One-Way ANOVA with Tukey's test.

Extended Data Fig. 9 | See next page for caption.
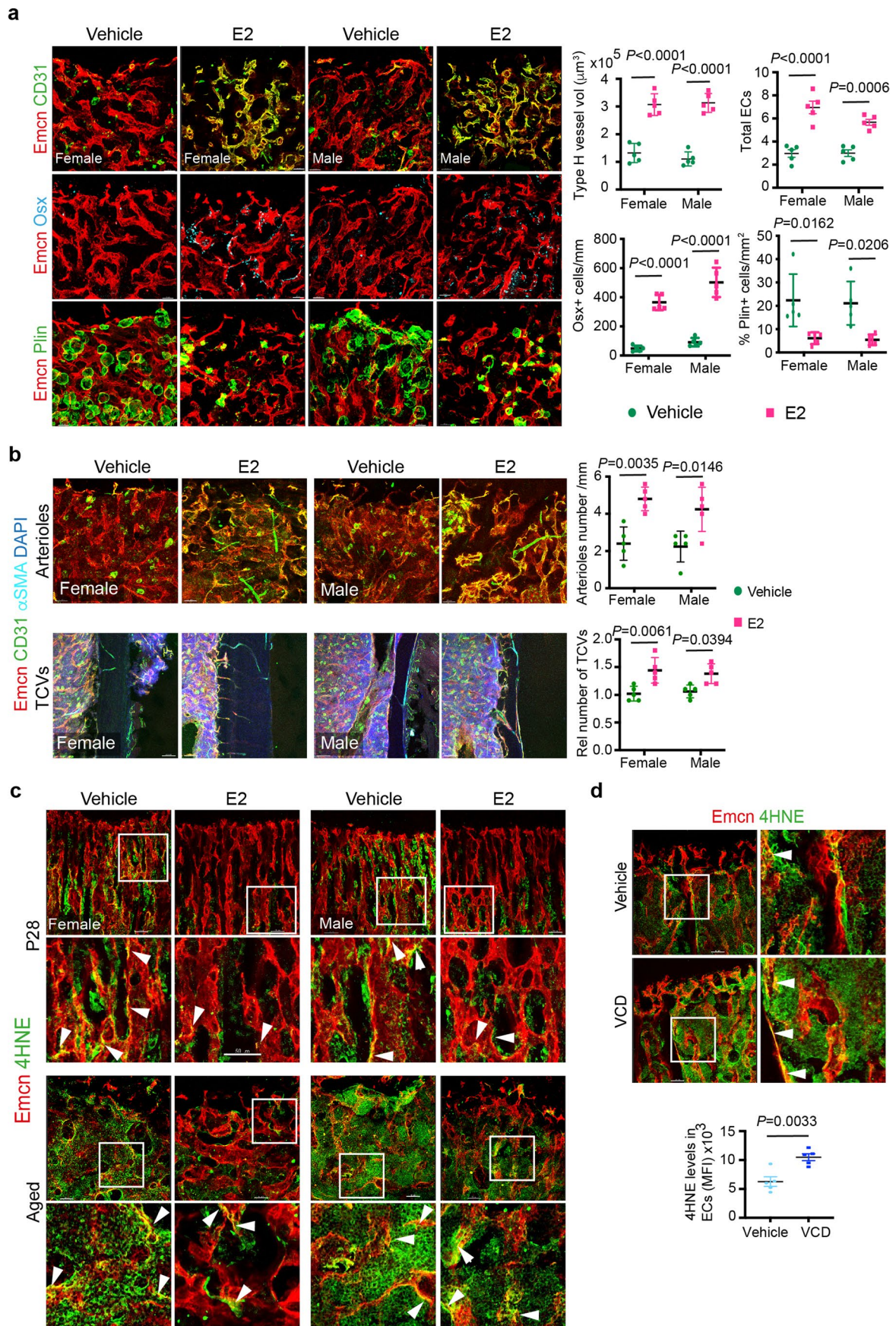
Extended Data Fig. 9 | Oestrogen recovers age-related bone loss. a, Representative confocal images show Type-H vessels (yellow, Emcn^{high} CD31^{high}), OBLs (Osterix+) and BM adipocytes (Perilipin+) in aged mice treated with E2 (Vehicle n = 5 F, n = 5 M; E2 n = 5 F, n = 5 M). Scale bars 40 μm. Graphs show quantification of total ECs, type-H vessels, Osx+ and Perilipin+ cells in bones of vehicle and E2 treated mice. Data are mean ± s.e.m. for flow cytometry data and mean ± s.d. for image quantification, Two-Way ANOVA with Tukey's test. **b**, Confocal images of bone sections immunostained for CD31 (green), endomucin (red), alpha-smooth muscle actin (αSMA, cyan) show distribution of CD31 + Emcn- arterioles and TCVs in aged mice treated with Vehicle and E2.

Quantification graphs show an increase in arterioles and TCVs (n = 5) after E2 administration in mice; Data are mean ± s.d.; Two-way ANOVA with Tukey's test. Scale bars 50 μm (arterioles), 100 μm (TCVs). **c**, Representative confocal images of 4HNE levels in bone endothelium of vehicle and E2-treated young (P28; n = 8) and aged (>60 weeks; n = 4) mice. Images show inset depicting endothelial expression of 4HNE illustrated by arrowheads. Scale bars 50 μm. **d**, VCD menopause model with insets indicating endothelial expression of 4HNE illustrated by arrowheads (Vehicle n = 5; VCD n = 5). Data are mean ± s.d.; Unpaired two-tailed t-test. Scale bars 50 μm.
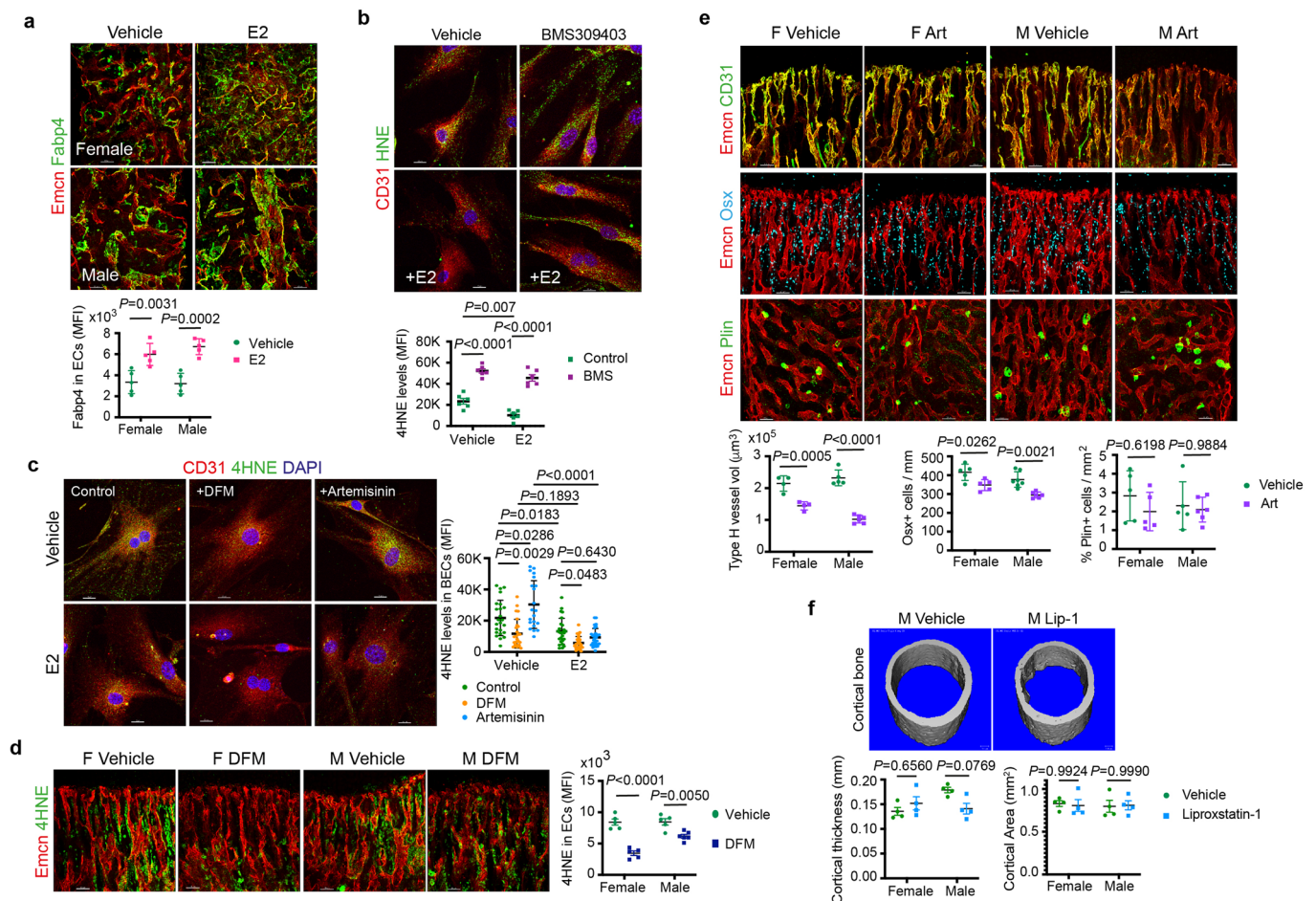
Extended Data Fig. 10 | Oestrogen recovers age-related bone loss. a, Representative confocal images of endothelial FABP4 expression in aged mice (n = 5), showing an increase after E2 treatment. Data are mean ± s.d.; Two-Way ANOVA with Tukey's test. Scale bars 50 µm. **b**, Representative confocal images with quantification of 4HNE levels in bone endothelial cells treated with vehicle and FABP4 inhibitor BMS 309403 in the presence of E2. Quantification showed high 4HNE levels upon FABP4 inhibition, which was not recovered by E2 treatment (n = 6). Data are mean ± s.d.; Two-Way ANOVA with Tukey's test. Scale bars 15 µm. **c**, Representative confocal images of BECs treated with Control, Deferoxamine (DFM) or Artemisinin (Art). Graph shows quantification of fluorescence intensity of endothelial 4HNE levels (Vehicle n = 24, E2 n = 26; Vehicle+DFM n = 26; E2 + DFM n = 27; Vehicle+Art n = 21; E2 + Art n = 23) Data are mean ± s.d.; Two-Way ANOVA with Tukey's test. Scale bars 15 µm. **d**, Representative confocal images with quantification of 4HNE levels in bone endothelium of vehicle (n = 5 F, n = 5 M) and DFM-treated mice (n = 5 F, n = 6 M) at P28. Data are mean ± s.d.; Two-Way ANOVA with Tukey's test. Scale bars 50 µm. **e**, Confocal images show type-H vessels, OBLs and perilipin expression in BM microenvironments of mice treated with Artemisinin (Art). Graphs showing quantification of Type-H vessel volume per field of mp (Vehicle n = 4 F, n = 5 M; Artemisinin n = 4 F, n = 6 M), Osterix+ cells per mm of mp (Vehicle n = 5 F, n = 7 M; Artemisinin n = 5 F, n = 6 M), and Perilipin+ area per mp area (Vehicle n = 5 F, n = 5 M; Artemisinin n = 5 F, n = 6 M). Data are mean ± s.d.; Two-Way ANOVA with Tukey's test. Scale bars 50 µm. **f**, Representative microCT 3D-rendered images show cortical bones of aged male mice treated with vehicle and Liproxstatin-1 (Lip-1). Graphs show cortical bone thickness (in mm) and cortical bone area of aged male and female mice treated with vehicle (n = 4 F, 4 M) and Liproxstatin-1 (n = 4 F, 4 M). Data are mean ± s.e.m.; Two-Way ANOVA with Tukey's test. Scale bars 100 µm.

nature portfolio

Corresponding author(s): Saravana Ramasamy

Last updated by author(s): 31st August 2022

Reporting Summary

Nature Portfolio wishes to improve the reproducibility of the work that we publish. This form provides structure for consistency and transparency in reporting. For further information on Nature Portfolio policies, see our Editorial Policies and the Editorial Policy Checklist.

Statistics

For all statistical analyses, confirm that the following items are present in the figure legend, table legend, main text, or Methods section.

n/a	Confirmed	
☐	☒	The exact sample size (n) for each experimental group/condition, given as a discrete number and unit of measurement
☐	☒	A statement on whether measurements were taken from distinct samples or whether the same sample was measured repeatedly
☐	☒	The statistical test(s) used AND whether they are one- or two-sided *Only common tests should be described solely by name; describe more complex techniques in the Methods section.*
☐	☒	A description of all covariates tested
☐	☒	A description of any assumptions or corrections, such as tests of normality and adjustment for multiple comparisons
☐	☒	A full description of the statistical parameters including central tendency (e.g. means) or other basic estimates (e.g. regression coefficient) AND variation (e.g. standard deviation) or associated estimates of uncertainty (e.g. confidence intervals)
☐	☒	For null hypothesis testing, the test statistic (e.g. F, t, r) with confidence intervals, effect sizes, degrees of freedom and P value noted *Give P values as exact values whenever suitable.*
☒	☐	For Bayesian analysis, information on the choice of priors and Markov chain Monte Carlo settings
☒	☐	For hierarchical and complex designs, identification of the appropriate level for tests and full reporting of outcomes
☒	☐	Estimates of effect sizes (e.g. Cohen's d, Pearson's r), indicating how they were calculated

Our web collection on statistics for biologists contains articles on many of the points above.

Software and code

Policy information about availability of computer code

Data collection	BD FACSDiva 9.0.0, Bio-RAD CFX Manager 3.1, Leica LASX (confocal imaging), QuantaSmart (Liquid Scintillation analyser), FLUOstar Omega Microplate reader 3.0, DESeq2.
Data analysis	FlowJo 10.7.1, Imaris Image Analysis Software 9.2, ImageJ (Fiji) 2.0.0, Adobe Illustrator 24.0.1, GraphPad Prism 8.0, Wave 2.6

For manuscripts utilizing custom algorithms or software that are central to the research but not yet described in published literature, software must be made available to editors and reviewers. We strongly encourage code deposition in a community repository (e.g. GitHub). See the Nature Portfolio guidelines for submitting code & software for further information.

Data

Policy information about availability of data

All manuscripts must include a data availability statement. This statement should provide the following information, where applicable:
- Accession codes, unique identifiers, or web links for publicly available datasets
- A description of any restrictions on data availability
- For clinical datasets or third party data, please ensure that the statement adheres to our policy

RNA sequencing data are deposited at GEO under accession number GSE163515 and GSE180246. All other data supporting the findings in this study are available as supplementary information.

Field-specific reporting

Please select the one below that is the best fit for your research. If you are not sure, read the appropriate sections before making your selection.

☒ Life sciences ☐ Behavioural & social sciences ☐ Ecological, evolutionary & environmental sciences

For a reference copy of the document with all sections, see nature.com/documents/nr-reporting-summary-flat.pdf

Life sciences study design

All studies must disclose on these points even when the disclosure is negative.

Sample size	No statistical testing was performed to predetermine sample sizes. Sample sizes were chosen from previously published data and experience with skeletal phenotypic analyses in transgenic animals that produce statistically significant results (Romeo et al., 2019; Ramasamy et al, 2016). Typically, full litters were used (6-10 pups) for analyses to ensure enough numbers for sex- and age- matching as well as control littermates for transgenic animals.
Data exclusions	Data were not excluded for analysis
Replication	Multiple (atleast two) independent experiments were performed to validate the reproducibility of the data producing similar results.
Randomization	No randomization was performed. Experiments involving wildype mice were performed on inbred mice from C57Bl6 background. Transgenic mice comparisons were done on litters from the same strain ensuring littermate controls to validate phenotypes.
Blinding	Blinding was not carried out as investigators have access to mouse data and regulated procedures need to be recorded in the animal facility. Animals were compared with the same sex and age and within the same strain.

Reporting for specific materials, systems and methods

We require information from authors about some types of materials, experimental systems and methods used in many studies. Here, indicate whether each material, system or method listed is relevant to your study. If you are not sure if a list item applies to your research, read the appropriate section before selecting a response.

Materials & experimental systems

n/a	Involved in the study
☐	☒ Antibodies
☐	☒ Eukaryotic cell lines
☒	☐ Palaeontology and archaeology
☐	☒ Animals and other organisms
☒	☐ Human research participants
☒	☐ Clinical data
☒	☐ Dual use research of concern

Methods

n/a	Involved in the study
☒	☐ ChIP-seq
☐	☒ Flow cytometry
☒	☐ MRI-based neuroimaging

Antibodies

Antibodies used	Endomucin (Santa Cruz Biotechnology;sc-65495; 1:100), Osterix (Abcam; ab22552; 1:600), CD31 (R&D Systems; AF3628; 1:100), Perilipin (Cell Signalling Technology; 9349S; 1:100), Perilipin (GeneTex; GTX89060; 1:100), anti-Ki67 (Abcam, ab16667, 1:100), Laminin (Sigma; L9393; 1:100), Fabp4 (R&D Systems, MAB4754; 1:100), anti-4-Hydroxynonenal (Abcam, ab46545; 1:200), HSL (Cell Signalling Technology; 4107; 1:50), ATGL (Cell Signalling Technology; 2138; 1:100), CD45 (BD Pharmingen, 553077; 1:100), Itgb3 (Cell Signalling Technology; FAB8557A; 1:100). Anti-rat Alexa Fluor 594 (Invitrogen; A21209, 1:400), anti-rat Alexa Fluor 488 (Invitrogen; A21208; 1:400), anti-goat Alexa Fluor 488 (Invitrogen; A11055, 1:400), anti-goat Alexa Fluor 546 (Invitrogen; A11056; 1:400), anti-goat Alexa Fluor 647 (Invitrogen; A21447; 1:400), anti- rabbit Alexa Fluor 488 (Invitrogen; A21206; 1:400), anti-rabbit Alexa Fluor 546 (Invitrogen; A10040; 1:400).
Validation	All antibodies used in this study are commercially available and have been widely used in publications as well as optimized in the lab. They have been validated for the immunohistochemistry studies and specificity for mice. The complete information and validation details are provided in the respective manufacturer's website data-sheets.

Eukaryotic cell lines

Policy information about cell lines

Cell line source(s)	mouse primary bone endothelial cells were cultured and used in the study

Authentication	cell lines were authenticated using endothelial cell markers expression.
Mycoplasma contamination	No mycoplasma testing was performed, as there was no contamination.
Commonly misidentified lines (See ICLAC register)	*Name any commonly misidentified cell lines used in the study and provide a rationale for their use.*

Animals and other organisms

Policy information about studies involving animals; ARRIVE guidelines recommended for reporting animal research

Laboratory animals	All wildtype animals were from C57Bl6 background, either purchased from Charles River Laboratories (CRL) or bred in-house. Transgenic mice were mixed background. Ovariectomised mice were C57Bl6 background and purchased from CRL. All mice were maintained in pathogen-free facilities with ad libitum food supply on a 12h light and dark cycle as per international guidelines. Experiments involving wildtype mice were on C57Bl6 background with both males and females age-matched for each experiment. Transgenic mice age- and sex-matched, were usually injected at post-natal day 10-14 and analysed at post-natal day 28. Adult mice were injected from post-natal day 66-70 and analysed at post-natal day 84. Aging experiments, using both sexes, were performed on mice over 65 weeks old.
Wild animals	No wild animals were used in this study
Field-collected samples	No samples were field-collected
Ethics oversight	All animal experiments were performed in accordance with the local ethical and care guidelines at the Imperial College London and the International guidelines of the Home Office (UK). The work is performed under the home office project licence no. PA5215DFC and PP3113493 granted to Dr. Saravana K Ramasamy.

Note that full information on the approval of the study protocol must also be provided in the manuscript.

Flow Cytometry

Plots

Confirm that:

[x] The axis labels state the marker and fluorochrome used (e.g. CD4-FITC).

[x] The axis scales are clearly visible. Include numbers along axes only for bottom left plot of group (a 'group' is an analysis of identical markers).

[x] All plots are contour plots with outliers or pseudocolor plots.

[x] A numerical value for number of cells or percentage (with statistics) is provided.

Methodology

Sample preparation	Long bones from mice were used for all experiments, either femurs or tibiae where each sample represents a bone from a distinct mouse. Bones were dissected and cleaned of all adhering muscle and crushed with a mortar and pestle in ice-cold PBS. RBC lysis was performed on total bone marrow cells to deplete erythrocytes, followed by collagenase digestion for 30 min at 37°C. Cells were then washed and filtered to obtain a single cell suspension, prior to antibody staining.
Instrument	Cells were acquired on the BD LSR II
Software	Data acquisition was done using BD FACSDiva 9.0 and data analysis was done using FlowJo 10.7.1
Cell population abundance	Abundance of cells was determined by distinct populations within negative and positive fractions upon antibody staining. Cells were highly positive for the endothelial marker CD31 after RBC removal as well as gating out the haematopoietic fraction (using CD45). Primary endothelial cells from the bone were also cultured in vitro and showed high specificity for CD31+ staining confirmed by high-resolution confocal microscopy.
Gating strategy	FSC/SSC gates were set for total bone marrow population due to the heterogeneity of multiple cell populations within the bone (excluding debris), followed by FSCA/H gates for gating single cell populations. This was followed by negative or positive antibody gates easily distinguished by the unstained population and using single antibody-only controls for CD45- and CD31+ populations respectively. Mitochondrial gates were determined by density of cell spread into 3 distinct populations. CD31high, Endomucinhigh and CD31low, Endomucinlow gates were based on previous published gating strategies as well as 2 distinct positive high and low populations.

[x] Tick this box to confirm that a figure exemplifying the gating strategy is provided in the Supplementary Information.